Journal of the Mechanics and Physics of Solids 97 (2016) 92–124

Contents lists available at ScienceDirect

Journal of the Mechanics and Physics of Solids

journal homepage: www.elsevier.com/locate/jmps

Second strain gradient elasticity of nano-objects

Nicolas M. Cordero [a,1], Samuel Forest [a,*], Esteban P. Busso [b]

[a] Mines ParisTech, Centre des Matériaux, CNRS UMR 7633, BP 87, 91003 Evry Cedex, France
[b] Onera, B.P. 80100, 91123 Palaiseau cedex, France

ARTICLE INFO

Article history:
Received 11 January 2015
Accepted 14 July 2015
Available online 21 July 2015

Keywords:
Third gradient elasticity
Second strain gradient
Surface energy
Surface stress
Micromorphic continuum
Nano-wire
Nano-porous material
Mechanics of nano-objects
Apparent elastic moduli

ABSTRACT

Mindlin's second strain gradient continuum theory for isotropic linear elastic materials is used to model two different kinds of size-dependent surface effects observed in the mechanical behaviour of nano-objects. First, the existence of an initial higher order stress represented by Mindlin's cohesion parameter, b_0, makes it possible to account for the relaxation behaviour of traction-free surfaces. Second, the higher order elastic moduli, c_i, coupling the strain tensor and its second gradient are shown to significantly affect the apparent elastic properties of nano-beams and nano-films under uni-axial loading. These two effects are independent from each other and allow for separated identification of the corresponding material parameters. Analytical results are provided for the size-dependent apparent shear modulus of a nano-thin strip under shear. Finite element simulations are then performed to derive the dependence of the apparent Young modulus and Poisson ratio of nano-films with respect to their thickness, and to illustrate hole free surface relaxation in a periodic nano-porous material.

1. Introduction

The elastic behaviour of nano-objects has attracted the attention of the scientific community in physics and mechanics with a view to probing the static and dynamic responses of nano-particles, nano-wires, nano-beams and nano-porous materials arising in various fields of engineering (Dingreville et al., 2005; Duan et al., 2009; Thomas et al., 2011). Evidence of size dependent behaviour of such nano-structures is mainly related to surface effects due to the fact that the ratio of their surface to volume becomes dominant. Thus most continuum models developed since the pioneering work of Gurtin and Murdoch (1975, 1978) introduce a membrane-like independent behaviour of surfaces and interfaces to account for both surface energy and surface stress effects (Müller and Saúl, 2004; Dingreville and Qu, 2008). Recent continuum mechanics advances in surface elasticity include extension to finite strain behaviour, a detailed description of edge and corner responses, thermal coupling and surface curvature effects (Javili and Steinmann, 2010; Chhapadia et al., 2011, 2012; Mohammadi et al., 2013; Javili et al., 2014).

Computational mechanical analysis of nano-objects is possible by means of finite element techniques to discretise the previous surface elasticity models, e.g. Yvonnet et al. (2011), Javili and Steinmann (2011), and Javili et al. (2014). Theoretical and computational surface elasticity can be specialised to the slender and thin bodies very often encountered in actual MEMS/NEMS applications. Beams, plate and shell models of solids endowed with surface energy and surface stress were

* Corresponding author.
E-mail addresses: nmcordero@gmail.com (N.M. Cordero), samuel.forest@ensmp.fr (S. Forest), esteban.busso@onera.fr (E.P. Busso).
[1] Now at Saint-Gobain Research, Aubervilliers, France.

http://dx.doi.org/10.1016/j.jmps.2015.07.012
0022-5096/

developed recently in Altenbach and Eremeyev (2011) and Altenbach et al. (2011, 2012).

Physical surface layers and interfaces are not actual infinitesimal surfaces but rather extended thin zones corresponding to the rows of atoms affected by specific boundary or interface conditions and compatibility requirements. In micro and nano-mechanical approaches, they can therefore be represented by layers of finite thickness, which is sometimes hard to be defined precisely, with specific elastic properties different from those of the bulk material, as done for instance in the context of the three-phase homogenisation model by Marcadon et al. (2007). Surface elasticity models then emerge as asymptotic limits of such layered nanostructures (He and Feng, 2012; Hervé-Luanco, 2014). Effective properties of composite materials with energetic and elastic interfaces can then be homogenised to determine their particle size-dependent properties (Javili et al., 2013; Gu et al., 2014).

Surface elasticity involves additional material parameters compared to the bulk constitutive behaviour. These parameters can be identified either from experimental nano-mechanical tests or from molecular dynamics or ab initio simulations. First principle simulations were used in Mitrushchenkov et al. (2010), Yvonnet et al. (2011, 2012), and Hoang et al. (2013) to identify the surface and bulk elastic properties of ZnO nano wires. Marcadon et al. (2013) and Davydov et al. (2013) resorted to molecular statics and dynamics for the identification of the surface-enhanced nano-structure and nano-composite behaviour. Nano-porous materials were also modelled by means of surface elasticity concepts in Duan et al. (2009) and Dormieux and Kondo (2013). Stability requirements for the surface elasticity moduli were discussed by Javili et al. (2012).

Alternative models for the size-dependent behaviour of materials are represented by generalised continua like higher grade media. The second gradient of displacement theory or, equivalently, the first strain gradient theory designed by Casal (1961, 1963), Toupin (1962), Mindlin (1964), and Mindlin and Eshel (1968) was early recognised as a candidate model to describe capillarity in elastic fluids and free surface effects in crystalline solids. This class of models has the advantage that it does not distinguish explicitly the surface from the bulk constitutive behaviour. Higher order elasticity moduli are introduced that enrich the bulk strain energy function. Surface effects then arise as a consequence of first and second order boundary conditions required by the higher grade continuum theories. The capability of the second gradient model to account for capillarity effects in fluids was discussed further by Casal (1972), Casal and Gouin (1985), Forest et al. (2011) and Auffray et al. (2013a). The numerous components of the sixth order tensor of first strain gradient elasticity were identified from atomic potentials in crystalline solids in Zhang and Sharma (2005), Maranganti and Sharma (2007), Boehme et al. (2007), whereas Shodja et al. (2012) resorted to ab initio simulations.

Higher grade continuum theories can be formulated either by means of the method of virtual power according to Germain (1973a,b) and Forest and Sievert (2003), or by extending the Cauchy method to enrich surface tractions as discussed by Dell'Isola and Seppecher (1995, 1997) and Dell'Isola et al. (2012). The application of symmetry conditions to the constitutive elasticity tensors in gradient continua leads to the definition of proper symmetry classes, as recently done by Olive and Auffray (2013, 2014) and Auffray et al. (2013b).

Mindlin (1965) showed in a milestone paper that the linear elastic isotropic first strain gradient theory is insufficient to describe internal strains and stresses that develop close to free surfaces. He claimed that their existence requires initial third order stresses to account for cohesion forces. The cohesion material property in an isotropic elastic second strain gradient medium is fully characterised by a single parameter, b_0, that can be linked to surface tension when considering the sharp interface limit. The need for a third displacement gradient or, equivalently, a second strain gradient theory, and the significance of the cohesion parameter b_0 were recently re-examined for elastic fluids by Forest et al. (2011) and for isotropic solids by Cordero (2011) and Ojaghnezhad and Shodja (2013). Mindlin's third displacement gradient/second strain gradient theory has been further developed recently to include dynamics effects (Polizzotto, 2013), and finite deformation (Javili et al., 2013). The higher order elastic moduli of an isotropic second strain gradient material were recently identified from ab initio simulations by Ojaghnezhad and Shodja (2013). Amiot (2013) showed that these higher order moduli can also be identified from measurements of cantilever sensors and MEMS/NEMS.

The connection between the elastic properties of second strain gradient materials and surface effects in nano-objects remains therefore a largely open question. The objective of the present paper is to demonstrate the capability of the second strain gradient model to account for not only surface energy but also for surface elasticity effects in some simple physical situations. Size-dependent apparent elastic properties of nano-wires will be defined and derived, for the first time, from the higher order elastic moduli of the second strain gradient theory. It will be shown that the considered second strain gradient theory generates two types of surface effects both linked to distinct sets of higher order elastic moduli. The solutions of several boundary value problems to be presented in this work will show that the moduli responsible for apparent surface energy and surface elasticity effects are independent and are related to distinct constitutive features of the continuum theory. Original analytical solutions of free standing films and shearing of a second strain gradient material strip will be provided. Finite element simulations are performed for the first time for the elastic tension/compression of a thin plate and for the computation of the free surface relaxation of a nano-porous periodic material. The question of the identification of the relevant material parameters from available experimental results for ZnO nano-wires is illustrated and discussed.

Mindlin's second strain gradient theory for isotropic solids is recalled in Section 2, insisting on the expression of balance and higher order traction conditions. The 18 first, second and third order elastic moduli arising from the theory are present in the constitutive relations that couple the first, second and third order stress tensors to the strain tensor and its first and second gradients. The problems of near-surface relaxation in a half-space and in a free-standing film, addressed by Ojaghnezhad and Shodja (2013), are solved in Section 3. Decaying, aperiodic and oscillating solutions are discussed depending on the values of higher order elastic moduli. The notion of apparent elastic property is introduced in the case of the

shearing of an infinite thin strip in Section 4. Exact solutions are derived for the apparent shear modulus as a function of the classical shear modulus, of the higher order moduli and of the strip thickness. A finite element implementation of second strain gradient elasticity is then proposed in Appendices A and B based on a constrained higher order micromorphic continuum theory. It is then applied in Section 5.1 to the study of the apparent Young modulus and Poisson ratio of a thin plate in tension. The free surface relaxation in a periodic nano-structured porous material is finally simulated in Section 5.2.

The notation to be henceforth used is as follows. The physical quantities introduced in the work share the same definitions and names as those in Mindlin's (1965) original work since the presented results heavily depend on Mindlin's major findings. The same notations were also used in a recent reference (Ojaghnezhad and Shodja, 2013). The theory is developed within the small deformation framework.

An intrinsic notation is used where zero, first, second, third and fourth order tensors are denoted by a, $\underline{\boldsymbol{a}}$, $\underset{\sim}{\boldsymbol{a}}$, $\underset{\simeq}{\boldsymbol{a}}$ and $\underset{\approx}{\boldsymbol{a}}$ respectively. The simple, double, triple and quadruple contractions are written ., :, ⋮ and :: respectively. A direct index notation with respect to an orthonormal Cartesian basis $(\underline{\boldsymbol{e}}_1, \underline{\boldsymbol{e}}_2, \underline{\boldsymbol{e}}_3)$ is also used for the sake of clarity. In particular,

$$\underline{\boldsymbol{a}}.\,\underline{\boldsymbol{b}} = a_i b_i, \quad \underset{\sim}{\boldsymbol{a}}:\,\underline{\boldsymbol{b}} = a_{ij} b_{ij}, \quad \underset{\simeq}{\boldsymbol{a}}\vdots\,\underset{\simeq}{\boldsymbol{b}} = a_{ijk} b_{ijk}, \quad \underset{\approx}{\boldsymbol{a}}::\,\underset{\approx}{\boldsymbol{b}} = a_{ijkl} b_{ijkl}, \tag{1}$$

where repeated indices are summed. Tensor product is denoted by $\otimes$ and the nabla operator is ∇. For example, the component ijk of $\underset{\sim}{\boldsymbol{a}} \otimes \nabla$ is $a_{ij,k}$. In particular, ∇^2 is the Laplace operator. As the formulated theories involve operations on tensors of order up to eight that may be unusual, both intrinsic and index notations are given to avoid any ambiguity. For instance, we give the chosen intrinsic and index notations for the second gradient of a scalar field and of a second rank tensor as

$$\nabla \otimes \nabla\rho = \rho_{,ij}\, \underline{\boldsymbol{e}}_i \otimes \underline{\boldsymbol{e}}_j, \quad \underset{\sim}{\boldsymbol{\varepsilon}} \otimes \nabla \otimes \nabla = \varepsilon_{ij,kl}\, \underline{\boldsymbol{e}}_i \otimes \underline{\boldsymbol{e}}_j \otimes \underline{\boldsymbol{e}}_k \otimes \underline{\boldsymbol{e}}_l. \tag{2}$$

2. Mindlin's second strain gradient elasticity theory

The balance and constitutive equations for isotropic second strain gradient elasticity as derived by Mindlin are presented next. The section ends with a discussion of the links between the cohesion parameter, b_0, and the concept of surface energy. The analysis is limited to static conditions in the absence of volume forces.

2.1. Balance equations and boundary conditions

Mindlin's third gradient material is an elastic solid endowed with an Helmholtz free energy density function that depends on the strain, strain gradient and second gradient of the strain tensors (Mindlin, 1965):

$$\rho\Psi = \rho\Psi\left(\underset{\sim}{\boldsymbol{\varepsilon}},\ \underset{\sim}{\boldsymbol{\varepsilon}} \otimes \nabla,\ \underset{\sim}{\boldsymbol{\varepsilon}} \otimes \nabla \otimes \nabla\right), \tag{3}$$

The theory can also be formulated in terms of the first, second and third gradients of the displacement field $\underline{\boldsymbol{u}}$:

$$\rho\Psi = \rho\tilde{\Psi}\left(\underset{\sim}{\boldsymbol{\varepsilon}},\ \underline{\boldsymbol{u}} \otimes \nabla \otimes \nabla,\ \underline{\boldsymbol{u}} \otimes \nabla \otimes \nabla \otimes \nabla\right), \tag{4}$$

Both formulations are equivalent due to compatibility requirements that imply bijective relationships between the strain gradient and the second gradient of the displacement field:

$$\varepsilon_{ij,k} = \frac{1}{2}\left(u_{i,jk} + u_{j,ik}\right), \tag{5a}$$

$$u_{i,jk} = \varepsilon_{ij,k} + \varepsilon_{ki,j} - \varepsilon_{jk,i}. \tag{5b}$$

Next, the theory is exploited in terms of strain and second and third gradients of the displacement field which are, respectively, denoted by

$$\begin{aligned} &\underset{\sim}{\boldsymbol{\varepsilon}} = \frac{1}{2}\left(\underline{\boldsymbol{u}} \otimes \nabla + \nabla \otimes \underline{\boldsymbol{u}}\right), \quad \underset{\simeq}{\boldsymbol{\varepsilon}} = \underline{\boldsymbol{u}} \otimes \nabla \otimes \nabla, \quad \underset{\approx}{\boldsymbol{\varepsilon}} = \underline{\boldsymbol{u}} \otimes \nabla \otimes \nabla \otimes \nabla, \\ &\varepsilon_{ij} = \frac{1}{2}\left(u_{i,j} + u_{j,i}\right), \quad \varepsilon_{ijk} = u_{i,jk}, \quad \varepsilon_{ijkl} = u_{i,jkl}, \end{aligned} \tag{6}$$

Then, Eq. (4) becomes

$$\rho\Psi = \rho\Psi\left(\underset{\sim}{\boldsymbol{\varepsilon}},\ \underset{\simeq}{\boldsymbol{\varepsilon}},\ \underset{\approx}{\boldsymbol{\varepsilon}}\right). \tag{7}$$

Alternative but equivalent formulations were listed by Mindlin and Eshel (1968) for the strain gradient theory. The classical infinitesimal strain tensor, $\underset{\sim}{\boldsymbol{\varepsilon}}$, is the symmetric part of the displacement field gradient and has six independent components in three dimensions (3D). The second gradient of the displacement field, $\underset{\simeq}{\boldsymbol{\varepsilon}}$, is symmetric in the last two indices and has eighteen independent components while the third gradient of the displacement field, $\underset{\approx}{\boldsymbol{\varepsilon}}$, is symmetric in the last three indices and has thirty independent components:

$$\varepsilon_{ij} = \varepsilon_{ji}, \quad \varepsilon_{ijk} = \varepsilon_{ikj}, \quad \varepsilon_{ijkl} = \varepsilon_{ijlk} = \varepsilon_{ikjl} = \varepsilon_{iklj} = \varepsilon_{iljk} = \varepsilon_{ilkj}. \tag{8}$$

In two dimensions (2D), these tensors have four, six and eight independent components, respectively.

The power density of internal forces of the third gradient continuum takes the form

$$\begin{aligned} p^{(i)}(\underset{\sim}{\dot{\varepsilon}}, \underline{\underline{\dot{\varepsilon}}}, \underset{\approx}{\dot{\varepsilon}}) &= \underset{\sim}{\sigma}\colon \underset{\sim}{\dot{\varepsilon}} + \underline{\underline{\boldsymbol{S}}} \vdots \underline{\underline{\dot{\varepsilon}}} + \underset{\approx}{\boldsymbol{S}} :: \underset{\approx}{\dot{\varepsilon}} \\ p^{(i)}(\dot{\varepsilon}_{ij}, \dot{\varepsilon}_{ijk}, \dot{\varepsilon}_{ijkl}) &= \sigma_{ij}\, \dot{\varepsilon}_{ij} + S_{ijk}\, \dot{\varepsilon}_{ijk} + S_{ijkl}\, \dot{\varepsilon}_{ijkl}, \end{aligned} \tag{9}$$

where

$$\begin{aligned} &\underset{\sim}{\sigma} = \rho \frac{\partial \Psi}{\partial \underset{\sim}{\varepsilon}}, \quad \underline{\underline{\boldsymbol{S}}} = \rho \frac{\partial \Psi}{\partial \underline{\underline{\varepsilon}}}, \quad \underset{\approx}{\boldsymbol{S}} = \rho \frac{\partial \Psi}{\partial \underset{\approx}{\varepsilon}}, \\ &\sigma_{ij} = \rho \frac{\partial \Psi}{\partial \varepsilon_{ij}}, \quad S_{ijk} = \rho \frac{\partial \Psi}{\partial \varepsilon_{ijk}}, \quad S_{ijkl} = \rho \frac{\partial \Psi}{\partial \varepsilon_{ijkl}}, \end{aligned} \tag{10}$$

are the generalised stress tensors and share the same symmetry properties as $\underset{\sim}{\varepsilon}$, $\underline{\underline{\varepsilon}}$ and $\underset{\approx}{\varepsilon}$, respectively. The mass volume density is ρ. The power of internal forces in a domain V, with smooth[2] boundary ∂V, can be expressed in terms of volume and surface contributions:

$$\begin{aligned} \mathcal{P}^{(i)} &= \int_V p^{(i)}\, dV = \int_V \left(\underset{\sim}{\sigma}\colon \underset{\sim}{\dot{\varepsilon}} + \underline{\underline{\boldsymbol{S}}} \vdots \underline{\underline{\dot{\varepsilon}}} + \underset{\approx}{\boldsymbol{S}} :: \underset{\approx}{\dot{\varepsilon}} \right) dV \\ &= \int_V \left[\underset{\sim}{\sigma}\colon \left(\underline{\boldsymbol{u}} \otimes \nabla \right) + \underline{\underline{\boldsymbol{S}}} \vdots \left(\underline{\boldsymbol{u}} \otimes \nabla \otimes \nabla \right) + \underset{\approx}{\boldsymbol{S}} :: \left(\underline{\boldsymbol{u}} \otimes \nabla \otimes \nabla \otimes \nabla \right) \right] dV \end{aligned} \tag{11}$$

$$\begin{aligned} = &- \int_V \left\{ \left[\underset{\sim}{\sigma} - \underline{\underline{\boldsymbol{S}}} \cdot \nabla + \underset{\approx}{\boldsymbol{S}} : \left(\nabla \otimes \nabla \right) \right] \cdot \nabla \right\} \cdot \underline{\boldsymbol{u}}\, dV + \int_{\partial V} \underline{\boldsymbol{n}} \cdot \left[\underset{\sim}{\sigma} - \underline{\underline{\boldsymbol{S}}} \cdot \nabla + \underset{\approx}{\boldsymbol{S}} : \left(\nabla \otimes \nabla \right) \right] \cdot \underline{\boldsymbol{u}}\, dS \\ &+ \int_{\partial V} \left\{ \left[\left(\underline{\underline{\boldsymbol{S}}} - \underset{\approx}{\boldsymbol{S}} \cdot \nabla \right) \cdot \underline{\boldsymbol{n}} + \underset{\approx}{\boldsymbol{S}} : \left(\underline{\boldsymbol{n}} \otimes \underline{\boldsymbol{L}} \right) - \left(\underset{\approx}{\boldsymbol{S}} \colon \left(\underline{\boldsymbol{n}} \otimes \underline{\boldsymbol{n}} \right) \right) \cdot \left(\underline{\boldsymbol{n}} \otimes \overset{t}{\underline{\boldsymbol{D}}} \right) \right) \cdot \underline{\boldsymbol{L}} \right\} \cdot \underline{\boldsymbol{u}}\, dS \\ &+ \int_{\partial V} \left[\left(\underline{\underline{\boldsymbol{S}}} - \underset{\approx}{\boldsymbol{S}} \cdot \nabla \right) \colon \left(\underline{\boldsymbol{n}} \otimes \underline{\boldsymbol{n}} \right) + \underset{\approx}{\boldsymbol{S}} \vdots \left(\underline{\boldsymbol{n}} \otimes \underline{\boldsymbol{L}} \otimes \underline{\boldsymbol{n}} \right) + \underset{\approx}{\boldsymbol{S}} \vdots \left(\underline{\boldsymbol{n}} \otimes \underline{\boldsymbol{n}} \otimes \underline{\boldsymbol{L}} \right) \right] \cdot \overset{n}{D} \underline{\boldsymbol{u}}\, dS \\ &+ \int_{\partial V} \left[\underset{\approx}{\boldsymbol{S}} \vdots \left(\underline{\boldsymbol{n}} \otimes \underline{\boldsymbol{n}} \otimes \underline{\boldsymbol{n}} \right) \right] \cdot \overset{n2}{D}\, \underline{\boldsymbol{u}}\, dS, \end{aligned} \tag{12}$$

$$\begin{aligned} \mathcal{P}^{(i)} = &- \int_V \left(\sigma_{ij,j} - S_{ijk,jk} + S_{ijkl,jkl} \right) \dot{u}_i\, dV + \int_{\partial V} \left(\sigma_{ij,j} - S_{ijk,jk} + S_{ijkl,jkl} \right) n_j\, \dot{u}_i\, dS \\ &+ \int_{\partial V} \left[L_j \left(S_{ijk} - S_{ijkl,l} \right) n_k + L_k L_l S_{ijkl}\, n_j - L_p S_{ijkl}\, n_j\, n_l \left(\overset{t}{D}_k n_p \right) \right] \dot{u}_i\, dS \\ &+ \int_{\partial V} \left(\left(S_{ijk} - S_{ijkl,l} \right) n_k\, n_j + L_l S_{ijkl}\, n_j\, n_k + L_k S_{ijkl}\, n_j\, n_l \right) \left(\overset{n}{D} \dot{u}_i \right) dS \\ &+ \int_{\partial V} S_{ijkl}\, n_j\, n_k\, n_l \left(\overset{n2}{D}\, \dot{u}_i \right) dS, \end{aligned} \tag{13}$$

where $\overset{n}{D}$, $\overset{t}{\underline{\boldsymbol{D}}}$ and $\underline{\boldsymbol{L}}$ are the surface differential operators introduced by Mindlin and defined in the following way: the gradient of $\underline{\boldsymbol{u}}$ on ∂V is decomposed into a normal gradient and a surface gradient:

$$\underline{\boldsymbol{u}} \otimes \nabla = \left(\overset{n}{D} \underline{\boldsymbol{u}} \right) \otimes \underline{\boldsymbol{n}} + \underline{\boldsymbol{u}} \otimes \overset{t}{\underline{\boldsymbol{D}}}, \quad \dot{u}_{i,j} = \overset{n}{D} \dot{u}_i\, n_j + \overset{t}{D}_j\, \dot{u}_i \tag{14}$$

The normal first and second gradient operators, $\overset{n}{D}$ and $\overset{n2}{D}$, are defined as

$$\overset{n}{D} \underline{\boldsymbol{u}} := \left(\underline{\boldsymbol{u}} \otimes \nabla \right) \cdot \underline{\boldsymbol{n}}, \quad \overset{n}{D} \dot{u}_i := \dot{u}_{i,k}\, n_k, \tag{15}$$

[2] The presence of edges and corners on the surface is excluded in the present work for simplicity. It is properly taken into account in the full theory by Mindlin (1965), Germain (1973a), and Javili et al. (2013).

$$\overset{n2}{D}\,\underline{\dot{\boldsymbol{u}}} := \left(\underline{\dot{\boldsymbol{u}}} \otimes \nabla \otimes \nabla\right) : \left(\underline{\boldsymbol{n}} \otimes \underline{\boldsymbol{n}}\right), \quad \overset{n2}{D}\,\dot{u}_i := \dot{u}_{i,kl}\, n_k\, n_l, \tag{16}$$

The surface gradient operator, $\underset{\sim}{\boldsymbol{D}}$, is expressed as

$$\underline{\dot{\boldsymbol{u}}} \otimes \overset{t}{\underline{\boldsymbol{D}}} := \left(\underline{\dot{\boldsymbol{u}}} \otimes \nabla\right) \cdot \left(\underset{\sim}{\boldsymbol{I}} - \underline{\boldsymbol{n}} \otimes \underline{\boldsymbol{n}}\right), \quad \overset{t}{D}_j\, \dot{u}_i := \dot{u}_{i,j} - \dot{u}_{i,k}\, n_k\, n_j. \tag{17}$$

Note that Eq. (14) can also be written in the following alternative form:

$$\begin{aligned} &\underline{\dot{\boldsymbol{u}}} \otimes \nabla = \left(\underline{\dot{\boldsymbol{u}}} \otimes \nabla\right) \cdot \left(\underline{\boldsymbol{n}} \otimes \underline{\boldsymbol{n}}\right) + \left(\underline{\dot{\boldsymbol{u}}} \otimes \nabla\right) \cdot \left(\underset{\sim}{\boldsymbol{I}} - \underline{\boldsymbol{n}} \otimes \underline{\boldsymbol{n}}\right), \\ &\dot{u}_{i,j} = \dot{u}_{i,k}\, n_k\, n_j + \dot{u}_{i,j} - \dot{u}_{i,k}\, n_k\, n_j. \end{aligned} \tag{18}$$

Mindlin's operator $\underline{\boldsymbol{L}}$ is expressed as a function of the surface gradient operator, $\overset{t}{D}$, by its action on a vector field $\underline{\boldsymbol{\phi}}$:

$$\begin{aligned} &\int_{\partial V} \underline{\boldsymbol{L}} \cdot \underline{\boldsymbol{\phi}}\, dS = \int_{\partial V} \left[\left(\overset{t}{\underline{\boldsymbol{D}}} \cdot \underline{\boldsymbol{n}}\right) \underline{\boldsymbol{\phi}} \cdot \underline{\boldsymbol{n}} - \overset{t}{\underline{\boldsymbol{D}}} \cdot \underline{\boldsymbol{\phi}}\right] dS, \\ &\int_{\partial V} L_l \phi_l\, dS = \int_{\partial V} \left[\left(\overset{t}{D}_m\, n_m\right) \phi_l\, n_l - \overset{t}{D}_l\, \phi_l\right] dS. \end{aligned} \tag{19}$$

The power of internal forces as expressed in Eq. (12) is the result of two successive integrations by parts applied to the initial form given in Eq. (11). The chain rule of differentiation and the divergence theorem are first applied. The decomposition (14) is then used in addition to the chain rule, surface integrations and the surface divergence theorem, see Mindlin (1965), in order to express $\mathcal{P}^{(i)}$ as a function of *the independent variations* $\underline{\dot{\boldsymbol{u}}}$, $\overset{n}{D}\underline{\dot{\boldsymbol{u}}}$ and $\overset{n2}{D}\,\underline{\dot{\boldsymbol{u}}}$.

The power of contact forces must therefore take the form

$$\mathcal{P}^{(ext)} = \int_{\partial V} \left(\overset{1}{\underline{\boldsymbol{t}}} \cdot \underline{\dot{\boldsymbol{u}}} + \overset{2}{\underline{\boldsymbol{t}}} \cdot \overset{n}{D}\underline{\dot{\boldsymbol{u}}} + \overset{3}{\underline{\boldsymbol{t}}} \cdot \overset{n2}{D}\,\underline{\dot{\boldsymbol{u}}}\right) dS \tag{20}$$

where $\overset{1}{\underline{\boldsymbol{t}}}$, $\overset{2}{\underline{\boldsymbol{t}}}$ and $\overset{3}{\underline{\boldsymbol{t}}}$ are generalised surface tractions.

The balance of momentum equations for the third gradient continuum, as deduced from the application of the principle of virtual power, reads

$$\begin{aligned} &\left[\underset{\sim}{\boldsymbol{\sigma}} - \underline{\underline{\boldsymbol{S}}} \cdot \nabla + \underline{\underline{\underline{\boldsymbol{S}}}} : \left(\nabla \otimes \nabla\right)\right] \cdot \nabla = 0 \\ &\sigma_{ij,j} - S_{ijk,jk} + S_{ijkl,jkl} = 0 \end{aligned} \tag{21}$$

The associated traction boundary conditions are

$$\begin{aligned} \overset{1}{\underline{\boldsymbol{t}}} = &\left[\underset{\sim}{\boldsymbol{\sigma}} - \underline{\underline{\boldsymbol{S}}} \cdot \nabla + \underline{\underline{\underline{\boldsymbol{S}}}} : \left(\nabla \otimes \nabla\right)\right] \cdot \underline{\boldsymbol{n}} + \left[\left(\underline{\underline{\boldsymbol{S}}} - \underline{\underline{\underline{\boldsymbol{S}}}} \cdot \nabla\right) \cdot \underline{\boldsymbol{n}} + \underline{\underline{\underline{\boldsymbol{S}}}} : \left(\underline{\boldsymbol{n}} \otimes \underline{\boldsymbol{L}}\right)\right. \\ &\left. - \left(\underline{\underline{\underline{\boldsymbol{S}}}} : \left(\underline{\boldsymbol{n}} \otimes \underline{\boldsymbol{n}}\right)\right) \cdot \left(\underline{\boldsymbol{n}} \otimes \overset{t}{\underline{\boldsymbol{D}}}\right)\right] \cdot \underline{\boldsymbol{L}} \end{aligned} \tag{22a}$$

$$\overset{2}{\underline{\boldsymbol{t}}} = \left(\underline{\underline{\boldsymbol{S}}} - \underline{\underline{\underline{\boldsymbol{S}}}} \cdot \nabla\right) : \left(\underline{\boldsymbol{n}} \otimes \underline{\boldsymbol{n}}\right) + \underline{\underline{\underline{\boldsymbol{S}}}} \vdots \left(\underline{\boldsymbol{n}} \otimes \underline{\boldsymbol{L}} \otimes \underline{\boldsymbol{n}}\right) + \underline{\underline{\underline{\boldsymbol{S}}}} \vdots \left(\underline{\boldsymbol{n}} \otimes \underline{\boldsymbol{n}} \otimes \underline{\boldsymbol{L}}\right) \tag{22b}$$

$$\overset{3}{\underline{\boldsymbol{t}}} = \underline{\underline{\underline{\boldsymbol{S}}}} \vdots \left(\underline{\boldsymbol{n}} \otimes \underline{\boldsymbol{n}} \otimes \underline{\boldsymbol{n}}\right). \tag{22c}$$

It is apparent in Eq. (20) that the corresponding Dirichlet conditions consist in prescribing the displacement and its first and second normal derivatives at the boundary.

2.2. Constitutive equations in isotropic linear elasticity

Mindlin (1965) derived the strain energy density for isotropic linear elastic second strain gradient materials as

Table 1
Physical dimensions of strains, stresses and elastic moduli used in the second strain gradient theory.

Coefficient	Dimension	Strain	Dimension	Stresses	Dimension
λ, μ	MPa $\equiv$ N mm^{-2}	ε_{ij}	dimensionless	σ_{ij}	MPa $\equiv$ N mm^{-2}
a_i, c_i, b_0	MPa mm^2 $\equiv$ N	ε_{ijk}	mm^{-1}	S_{ijk}	MPa mm $\equiv$ N mm^{-1}
$b_{i,\, i\neq 0}$	MPa mm^4 $\equiv$ N mm^2	ε_{ijkl}	mm^{-2}	S_{ijkl}	MPa mm^2 $\equiv$ N

$$\begin{aligned}\rho\Psi(\varepsilon_{ij},\,\varepsilon_{ijk},\,\varepsilon_{ijkl}) = {}& \tfrac{1}{2}\,\lambda\,\varepsilon_{ii}\,\varepsilon_{jj} + \mu\,\varepsilon_{ij}\,\varepsilon_{ij} + a_1\,\varepsilon_{iij}\,\varepsilon_{kkj} + a_2\,\varepsilon_{ijj}\,\varepsilon_{kki} + a_3\,\varepsilon_{ijj}\,\varepsilon_{ikk}\\ &+ a_4\,\varepsilon_{ijk}\,\varepsilon_{ijk} + a_5\,\varepsilon_{ijk}\,\varepsilon_{jik} + b_1\,\varepsilon_{iijj}\,\varepsilon_{kkll} + b_2\,\varepsilon_{iikl}\,\varepsilon_{jjkl}\\ &+ b_3\,\varepsilon_{ijkk}\,\varepsilon_{llji} + b_4\,\varepsilon_{ijkk}\,\varepsilon_{jill} + b_5\,\varepsilon_{ijkk}\,\varepsilon_{ijll} + b_6\,\varepsilon_{ijkl}\,\varepsilon_{ijkl}\\ &+ b_7\,\varepsilon_{ijkl}\,\varepsilon_{jkli} + c_1\,\varepsilon_{ii}\,\varepsilon_{jjkk} + c_2\,\varepsilon_{ij}\,\varepsilon_{kkij} + c_3\,\varepsilon_{ij}\,\varepsilon_{jikk} + b_0\,\varepsilon_{iijj}.\end{aligned} \tag{23}$$

Sixteen elasticity moduli arise in the free energy function in addition to the usual Lamé constants, λ and μ. The following distinction can be made among the numerous terms in Eq. (23):

- The five parameters, a_i, are the higher order elasticity moduli related to the second gradient of displacement or, equivalently, first strain gradient part of the theory, as derived by Toupin and Mindlin (Toupin, 1962; Mindlin, 1964).
- The seven parameters, $b_{i,\, i\neq 0}$, are the higher order elasticity moduli specifically related to the second strain gradient.
- The three parameters, c_i, are coupling moduli responsible for the coupling between the strain and the third gradient of the displacement field.
- The initial higher order stress or cohesion modulus, b_0, is related to the surface energy, as proved in Mindlin (1965).

It will be shown that the surface effects of interest in this work are related to the coupling moduli, c_i, and to the initial higher order stress, b_0, all appearing in the third order terms of the theory. The physical dimensions of the newly introduced moduli and of the strain and stress components are given in Table 1. The constitutive equations are obtained from the free energy density (23) and the definitions (10). They read

$$\sigma_{pq} = \lambda\,\varepsilon_{ii}\,\delta_{pq} + 2\,\mu\,\varepsilon_{pq} + c_1\,\varepsilon_{iijj}\,\delta_{pq} + c_2\,\varepsilon_{iipq} + \tfrac{1}{2}\,c_3\Big(\varepsilon_{pqii} + \varepsilon_{qpii}\Big), \tag{24a}$$

$$\begin{aligned}S_{pqr} = {}& a_1\Big(\varepsilon_{iir}\,\delta_{pq} + \varepsilon_{iiq}\,\delta_{pr}\Big) + \tfrac{1}{2}\,a_2\Big(\varepsilon_{rii}\,\delta_{pq} + 2\,\varepsilon_{iip}\,\delta_{qr} + \varepsilon_{qii}\,\delta_{pr}\Big)\\ &+ 2\,a_3\,\varepsilon_{pii}\,\delta_{qr} + 2\,a_4\,\varepsilon_{pqr} + a_5\Big(\varepsilon_{qrp} + \varepsilon_{rqp}\Big),\end{aligned} \tag{24b}$$

$$\begin{aligned}S_{pqrs} = {}& \tfrac{2}{3}\,b_1\,\varepsilon_{iijj}\,\delta_{pqrs} + \tfrac{2}{3}\,b_2\,\varepsilon_{iijk}\,\delta_{jkpqrs} + \tfrac{1}{6}\,b_3\Big(\big(\varepsilon_{jkii} + \varepsilon_{kjii}\big)\delta_{jkpqrs} + 2\varepsilon_{iijp}\,\delta_{jqrs}\Big)\\ &+ \tfrac{2}{3}\,b_4\,\varepsilon_{jpii}\,\delta_{jqrs} + \tfrac{2}{3}\,b_5\,\varepsilon_{pjii}\,\delta_{jqrs} + 2\,b_6\,\varepsilon_{pqrs} + \tfrac{2}{3}\,b_7\Big(\varepsilon_{qrsp} + \varepsilon_{rspq} + \varepsilon_{spqr}\Big)\\ &+ \tfrac{1}{3}\,c_1\,\varepsilon_{ii}\,\delta_{pqrs} + \tfrac{1}{3}\,c_2\,\varepsilon_{ij}\,\delta_{ijpqrs} + \tfrac{1}{3}\,c_3\,\varepsilon_{ip}\,\delta_{iqrs} + \tfrac{1}{3}\,b_0\,\delta_{pqrs},\end{aligned} \tag{24c}$$

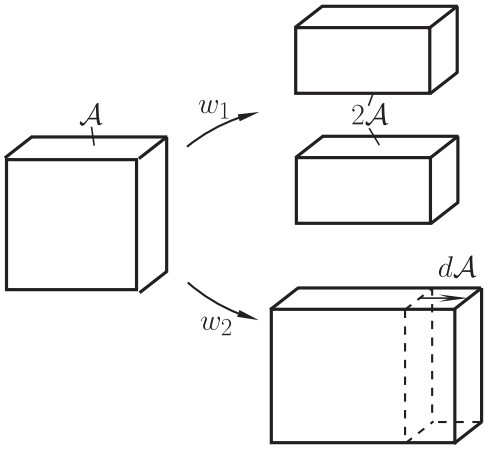

Fig. 1. A schematic representation of the two types of effects studied in this work arising at the surface or interface in solids. Here, w_1 and w_2 are the reversible works per unit area needed to create either a new surface or to elastically stretch an existing one, respectively. Then, the upper path illustrates the concepts of *surface energy* and the lower path of *surface stress*, according to Müller and Saúl (2004).

where fourth and sixth order identity tensors are defined as

$$\delta_{ijkl} = \delta_{ij}\delta_{kl} + \delta_{ik}\delta_{jl} + \delta_{jk}\delta_{il}, \quad \delta_{ijklmn} = \delta_{im}\delta_{jn}\delta_{kl} + \delta_{il}\delta_{jn}\delta_{km} + \delta_{il}\delta_{jm}\delta_{kn} \tag{25}$$

with δ_{ij} being the Kronecker symbol.

2.3. Surface energy

The last term in the free energy density equation (23), $b_0\ \varepsilon_{ijj}$, generates the components of the cohesive force, $1/3\ b_0\ \delta_{pqrs}$ in Eq. (24c). This self-equilibrating force is controlled by the initial higher order stress, b_0, and was shown by Mindlin to be directly linked to surface energy defined as the energy per unit area needed to create a new surface (see Fig. 1 as a reminder).

The effect of the modulus b_0 can be illustrated in the following simple situation. Let us consider a traction-free surface where the generalised surface tractions must vanish, in particular we have $\underline{\overset{3}{\boldsymbol{t}}} = 0$ which, with Eq. (22c), leads to $S_{ijkl}\ n_j\ n_k\ n_l = 0$ at the considered surface. If b_0 is non-vanishing, strains and/or higher order strains must exist in Eq. (24c) to counteract the cohesion force and lead to a vanishing higher order traction, $\underline{\overset{3}{\boldsymbol{t}}}$. As a result, the initial higher order stress induces straining at the free surface.

More specifically, in the absence of external load, i.e., when $\underline{\overset{1}{\boldsymbol{t}}} = \underline{\overset{2}{\boldsymbol{t}}} = \underline{\overset{3}{\boldsymbol{t}}} = 0$, the surface energy at the surface was derived point-wise by Mindlin (1965) as

$$\gamma = \tfrac{1}{2}\, b_0\, \overset{n}{D}\left(\underline{\boldsymbol{u}}\cdot\nabla\right), \quad \gamma = \tfrac{1}{2}\, b_0\, u_{i,ij}\, n_j \text{ on } \partial V \tag{26}$$

and is half the product of b_0 and the normal gradient of the dilatation at the surface, $\overset{n}{D}(\underline{\boldsymbol{u}}\cdot\nabla)$.

As discussed in Forest et al. (2011), such initial value of higher order stress cannot exist in the first strain gradient theory since an initial value of the third order hyperstress tensor, $\underset{\approx}{\boldsymbol{S}}_0$, would vanish for isotropic solids. It may however exist in anisotropic first gradient media as first recognised by Toupin (1962). Initial cohesion stresses in isotropic linear elastic solids then arise in second strain gradient media for the fourth order stress tensor $\underset{\approx}{\boldsymbol{S}}$. The consideration of material isotropy in gradient continua therefore gives credit to the third gradient continuum for a general representation of surface energy effects in solids.

The current theory is shown in the following to generate two types of surface effect both linked to distinct specific higher order moduli and therefore uncorrelated. The surface energy is then related to the initial higher order stress, or cohesion modulus, b_0, while the surface stress effects will be shown to be related to the coupling moduli, c_i (see Eq. (23)).

3. Surface energy effects in third gradient elasticity

In this section, surface energy related effects are evidenced in two simple boundary value problems involving free surfaces. The detailed analytical solutions also provide expressions of several characteristic lengths defined as functions of the isotropic elasticity moduli (23). Corresponding stability requirements are discussed. These are essentially one-dimensional solutions which involve several intrinsic lengths and dimensionless parameters that will be used in Section 4.

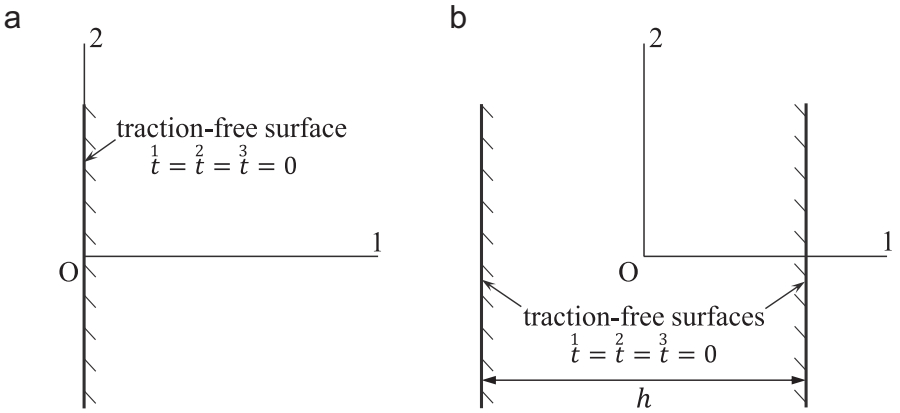

Fig. 2. Description of (a) the half-space, $x_1 \geq 0$, occupied by an elastic second strain gradient material with the plane surface $x_1 = 0$ assumed to be traction-free and of (b) the material strip located at $[-h/2, h/2]$, infinite along direction 2 and with the surfaces $x_1 = \pm h/2$ assumed to be traction-free.

3.1. Half-space with a free surface

The half-space, $x_1 \geq 0$, in a Cartesian coordinate system $\{x_1, x_2, x_3\}$ is occupied by an elastic second strain gradient material as described in Fig. 2.

In continuum mechanics, free surfaces are associated with Neumann conditions of vanishing tractions. In the context of a second strain gradient theory, the planar surface, $x_1 = 0$, is traction-free if

$$\underset{\sim}{\overset{1}{\boldsymbol{t}}} = \underset{\sim}{\overset{2}{\boldsymbol{t}}} = \underset{\sim}{\overset{3}{\boldsymbol{t}}} = 0 \quad \text{at } x_1 = 0. \tag{27}$$

We look for displacement fields of the form

$$u_1 = u_1(x_1), \quad u_2 = u_3 = 0. \tag{28}$$

The current problem is then essentially one-dimensional. The stress-equation of equilibrium (21) becomes

$$\sigma_{11,1} - S_{111,11} + S_{1111,111} = 0 \tag{29}$$

in the absence of body forces. The boundary conditions (22) then become

$$\sigma_{11} - S_{111,1} + S_{1111,11} = 0, \quad S_{111} - S_{1111,1} = 0, \quad S_{1111} = 0 \ \text{ at } x_1 = 0 \tag{30}$$

as the terms with surface gradients (i.e., with the operators $\underset{\sim}{\overset{t}{\boldsymbol{D}}}$ or $\underset{\sim}{\boldsymbol{L}}$) in (22) vanish in the case of the present flat surface. With the assumed displacement field Equation (28), the potential energy density (23) is a function of the strain components ε_{11}, ε_{111} and ε_{1111} only. Thus,

$$\rho\Psi\Big(\varepsilon_{11},\ \varepsilon_{111},\ \varepsilon_{1111}\Big) = \Big(\frac{\lambda}{2} + \mu\Big)\varepsilon_{11}^2 + \frac{A}{2}\,\varepsilon_{111}^2 + \frac{B}{2}\,\varepsilon_{1111}^2 + \bar{c}\ \varepsilon_{11}\,\varepsilon_{1111} + b_0\ \varepsilon_{1111} \tag{31}$$

with the following notations for reduced moduli,

$$A = 2(a_1 + a_2 + a_3 + a_4 + a_5), \quad B = 2(b_1 + b_2 + b_3 + b_4 + b_5 + b_6 + b_7), \quad \bar{c} = c_1 + c_2 + c_3. \tag{32}$$

From Table 1, it can be seen that the constants A and $\bar{c}$ have the dimension of forces (N) and B has the dimension of force times unit surface (N mm^2). The material parameters L_1 and L_2 with the dimension of length are now defined, together with the dimensionless parameters η and η_0:

$$L_1^2 = \frac{A}{\lambda/2 + \mu}, \quad L_2^2 = \frac{B}{A}, \quad \eta = \frac{\bar{c}}{A}, \quad \eta_0 = \frac{b_0}{A}. \tag{33}$$

The next objective here is to rewrite the potential energy density, Eq. (31), as a function of three dimensionless arguments. Hence,

$$\rho\Psi\Big(\varepsilon_{11},\ \varepsilon_{111},\ \varepsilon_{1111}\Big) = \rho\hat{\Psi}\Big(\varepsilon_{11},\ L_1\,\varepsilon_{111},\ L_2^2\,\varepsilon_{1111}\Big). \tag{34}$$

Note that the local stability of the material behaviour is ensured when the function $\hat{\Psi}(x, y, z)$ is convex with respect to its arguments. This implies the following requirements:

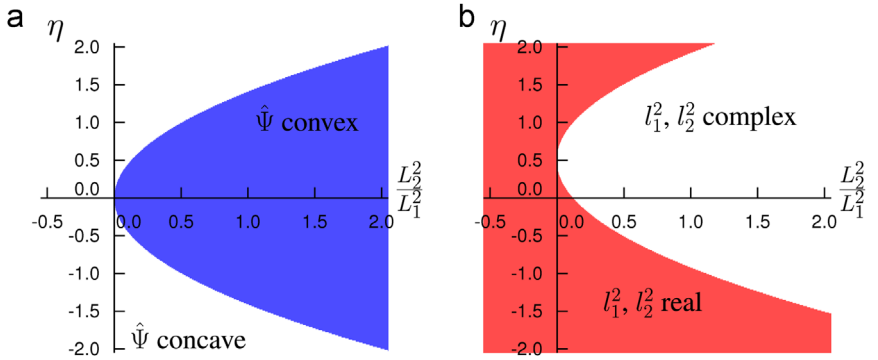

Fig. 3. Effects of the material parameters η and L_2^2/L_1^2: (a) stability requirements; the potential $\hat{\Psi}$ is convex for the sets of material parameters taken in the coloured area. (b) Set of l_1^2 and l_2^2: the square of the characteristic lengths l_1 and l_2 can either be complex or real depending on the sign of the part under the square root in Eqs. (39) and (40). The coloured area corresponds to the sets of material parameters for which l_1^2 and l_2^2 are real. (For interpretation of the references to colour in this figure caption, the reader is referred to the web version of this paper.)

$$L_1^2 \geq 0, \quad L_2^2 \geq 0, \quad 2\,\frac{L_2^2}{L_1^2} \geq \eta^2. \tag{35}$$

Recalling the expressions of the material parameters (33), these requirements impose that the moduli A and B are positive; however the modulus $\bar{c}$ can be either positive or negative. These will be used as a guideline to choose physically relevant material parameters for the theory. No condition for the initial higher order stress, b_0, arises from the convexity and this material parameter can be calibrated using the expression of the point surface energy given by Eq. (26). The requirements (35) are summarised in Fig. 3(a) where the coloured area represents the values of the material parameters η and L_2^2/L_1^2, which lead to a convex potential, $\hat{\Psi}$. The chosen notations in Eq. (33) provide a convenient description of the material parameters: L_1 and L_2 are related to the first and second strain gradients, respectively, and the ratio L_2^2/L_1^2 represents their relative weight, η describes the coupling between strain and the third gradient of displacement.

Combining Eqs. (10), (28) and (24), the components σ_{11}, S_{111} and S_{1111} of the stress tensors are derived:

$$\sigma_{11} = (\lambda + 2\mu)\varepsilon_{11} + \bar{c}\ \varepsilon_{1111}, \tag{36a}$$

$$S_{111} = A\ \varepsilon_{111}, \tag{36b}$$

$$S_{1111} = B\ \varepsilon_{1111} + \bar{c}\ \varepsilon_{11} + b_0. \tag{36c}$$

Substituting these expressions into the stress-equation of equilibrium (29) and recalling that $\varepsilon_{11} = u_{1,1}$, $\varepsilon_{111} = u_{1,111}$ and $\varepsilon_{1111} = u_{1,111}$, the following sixth order displacement-equation of equilibrium is derived:

$$\left(1 - l_1^2\,\frac{d^2}{dx_1^2}\right)\left(1 - l_2^2\,\frac{d^2}{dx_1^2}\right)\frac{d^2u_1}{dx_1^2} = 0. \tag{37}$$

It involves new characteristic lengths defined in the same way as in Mindlin (1965), namely,

$$l_1^2 l_2^2 = \frac{B}{\lambda + 2\mu}, \quad l_1^2 + l_2^2 = \frac{A - 2\bar{c}}{\lambda + 2\mu}, \tag{38}$$

from which the individual intrinsic lengths, l_1 and l_2, can be obtained:

$$l_1^2 = \frac{A - 2\bar{c} + \sqrt{(A - 2\bar{c})^2 - 4B\left(\lambda + 2\mu\right)}}{2(\lambda + 2\mu)}, \quad l_2^2 = \frac{A - 2\bar{c} - \sqrt{(A - 2\bar{c})^2 - 4B\left(\lambda + 2\mu\right)}}{2(\lambda + 2\mu)}, \tag{39}$$

or alternatively:

$$l_1^2 = \frac{L_1^2}{4}\left(1 - 2\eta + \sqrt{(1 - 2\eta)^2 - 8\frac{L_2^2}{L_1^2}}\right), \quad l_2^2 = \frac{L_1^2}{4}\left(1 - 2\eta - \sqrt{(1 - 2\eta)^2 - 8\frac{L_2^2}{L_1^2}}\right), \tag{40}$$

using the previously defined characteristic lengths L_1 and L_2. The solution of (37) then has the general form:

$$u_1(x_1) = \alpha_1\, e^{x_1/l_1} + \alpha_2\, e^{-x_1/l_1} + \alpha_3\, e^{x_1/l_2} + \alpha_4\, e^{-x_1/l_2} + \alpha_5\, x_1 + \alpha_6. \tag{41}$$

The different types of material responses that can be described by these solutions are now discussed. The characteristic lengths l_1 and l_2 must be considered as complex numbers. Then, the exponentials $e^{\pm x_1/l_1}$ and $e^{\pm x_1/l_2}$ in the solution of the displacement-equation of equilibrium (41) can alternatively correspond to hyperbolic functions if both l_1 and l_2 are real

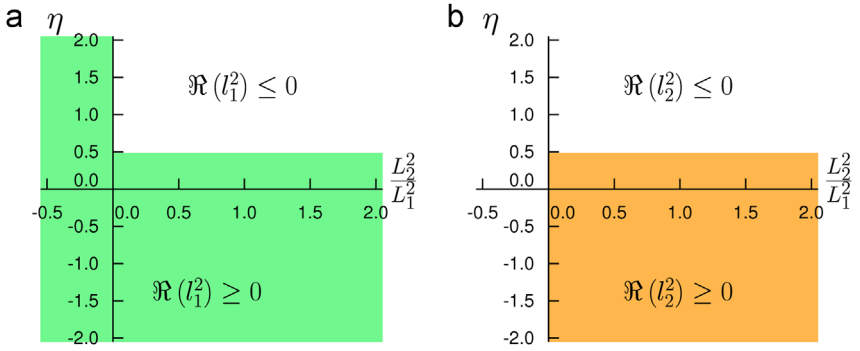

Fig. 4. Sign of (a) $\Re\left(l_1^2\right)$ and (b) $\Re\left(l_2^2\right)$: the coloured areas correspond to the sets of material parameters for which the real part of the square of the lengths l_1 and l_2 is positive. These results are obtained with L_1^2 positive. (For interpretation of the references to colour in this figure caption, the reader is referred to the web version of this paper.)

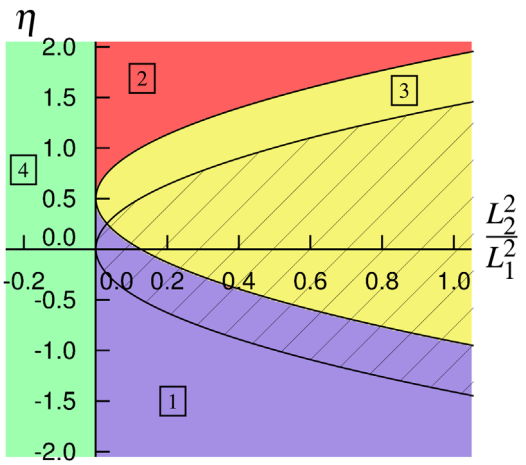

Fig. 5. Summary of the four main cases predicted by the theory. Only the sets of material parameters taken in areas "1" and "3" lead to solutions vanishing at infinity. The hatched area represents the convex domain described by the requirements (35). This convex domain is associated with both exponential and aperiodic physically relevant behaviour (i.e., convex domain $\subset 1 \cup 3$).

numbers, trigonometric functions if both l_1 and l_2 are imaginary numbers, or aperiodic functions if both real and imaginary parts of l_1 and l_2 are non-zero.

A study of the expressions of these characteristic lengths (39) or (40) is needed to know the form of the solution for a given set of material parameters and then to fully understand the 1D material behaviour. For that purpose, the sign of the part $(A-2\bar{c})^2-4B\left(\lambda+2\mu\right)$ or, equivalently, $(1-2\eta)^2-8L_2^2/L_1^2$ under the square root in both expressions (39) and (40) must be considered: if it is positive, l_1^2 and l_2^2 are real; if not, l_1^2 and l_2^2 are complex numbers. These two possibilities are represented in Fig. 3(b). Similarly, the sign of the real part of l_1^2 and l_2^2, represented in Fig. 4, has a strong impact on the resulting behaviour. The various cases arising from the combination of the previous conclusions are summarised in Fig. 5:

1. If l_1^2 and l_2^2 are real (i.e., $\Im(l_1^2, l_2^2)=0$) and if l_1^2 and l_2^2 are positive, then l_1 and l_2 are real and the solution of the displacement-equation of equilibrium (41) becomes

$$u_1(x_1)=\alpha_2\, e^{-x_1/l_1}+\alpha_4\, e^{-x_1/l_2} \tag{42}$$

as the considered case is semi-infinite and therefore requires a solution vanishing at infinity. Eq. (42) is given in the case of positive characteristic lengths l_1 and l_2, the exponentials vanishing at infinity being e^{-x_1/l_1} and e^{-x_1/l_2}. With negative l_1 and l_2, the two remaining terms in the solution of the displacement-equation of equilibrium, would be the terms with α_1 and α_3 with the vanishing exponentials e^{x_1/l_1} and e^{x_1/l_2}. Eq. (42) can also be written as

$$u_1(x_1)=\alpha_2\left[\cosh\left(\frac{x_1}{l_1}\right)-\sinh\left(\frac{x_1}{l_1}\right)\right]+\alpha_4\left[\cosh\left(\frac{x_1}{l_2}\right)-\sinh\left(\frac{x_1}{l_2}\right)\right]. \tag{43}$$

It describes an exponential decrease of the surface effects as the distance from the traction-free surface increases. This case corresponds to the area "1" of Fig. 5.

2. If l_1^2 and l_2^2 are real and if l_1^2 and l_2^2 are negative, then l_1 and l_2 (and consequently, α_1, α_2, α_3 and α_4) are imaginary (i.e., $\Re(l_1, l_2)=0$, $\Im(l_1, l_2)\neq 0$) and (41) can be written as

$$\begin{aligned} u_1(x_1)=\Re\Bigg\{&\alpha_1\left[\cos\left(\frac{ix_1}{l_1}\right)-i\,\sin\left(\frac{ix_1}{l_1}\right)\right]+\alpha_2\left[\cos\left(\frac{ix_1}{l_1}\right)+i\,\sin\left(\frac{ix_1}{l_1}\right)\right]\\ &+\alpha_3\left[\cos\left(\frac{ix_1}{l_2}\right)-i\,\sin\left(\frac{ix_1}{l_2}\right)\right]+\alpha_4\left[\cos\left(\frac{ix_1}{l_2}\right)+i\,\sin\left(\frac{ix_1}{l_2}\right)\right]\Bigg\}, \end{aligned} \tag{44a}$$

$$\begin{aligned} u_1(x_1)=&\Im\left(\alpha_1\right)\sin\left(\frac{x_1}{\Im(l_1)}\right)-\Im\left(\alpha_2\right)\sin\left(\frac{x_1}{\Im(l_1)}\right)+\Im\left(\alpha_3\right)\sin\left(\frac{x_1}{\Im(l_2)}\right)\\ &-\Im\left(\alpha_4\right)\sin\left(\frac{x_1}{\Im(l_2)}\right). \end{aligned} \tag{44b}$$

This solution, which oscillates, does not vanish at infinity and has no physical meaning for the half-space problem. The sets of material parameters, corresponding to area "2" of Fig. 5, are therefore excluded.

3. If l_1^2 and l_2^2 are complex numbers (i.e., $\Re(l_1, l_2) \neq 0$, $\Im(l_1, l_2) \neq 0$), l_1 and l_2 are complex as well and (41) can be written as

$$u_1(x_1) = e^{-x_1\Re(l_1)/(\Re(l_1)^2+\Im(l_1)^2)}\left[\Re(\alpha_2)\cos\left(\frac{x_1\Im(l_1)}{\Re(l_1)^2+\Im(l_1)^2}\right) - \Im(\alpha_2)\sin\left(\frac{x_1\Im(l_1)}{\Re(l_1)^2+\Im(l_1)^2}\right)\right]$$
$$+ e^{-x_1\Re(l_2)/(\Re(l_2)^2+\Im(l_2)^2)}\left[\Re(\alpha_4)\cos\left(\frac{x_1\Im(l_2)}{\Re(l_2)^2+\Im(l_2)^2}\right) - \Im(\alpha_4)\sin\left(\frac{x_1\Im(l_2)}{\Re(l_2)^2+\Im(l_2)^2}\right)\right], \tag{45}$$

with $\Re(l_1)$ and $\Re(l_2)$ being positive, ensuring that $u_1(x_1)$ vanishes at infinity. A similar solution exists with $\Re(l_1)$ and $\Re(l_2)$ being negative, the remaining terms are then the terms with α_1 and α_3 of Eq. (41). Here, the oscillating solution decreases exponentially so that the surface effects remain localised in the traction-free surface region. This case corresponds to material parameters taken in area "3" of Fig. 5.

4. The last case corresponds to area "4". It is obtained with l_1^2 and l_2^2 being real and of opposite signs leading to l_1 real and l_2 imaginary. The solution takes the form of a sum of an exponential and a trigonometric function,

$$u_1(x_1) = \Re(\alpha_1)\, e^{x_1/l_1} + \Re(\alpha_2)\, e^{-x_1/l_1} + \Re(\alpha_3)\cos\left(\frac{x_1}{\Im(l_2)}\right) + \Im(\alpha_3)\sin\left(\frac{x_1}{\Im(l_2)}\right)$$
$$+ \Re(\alpha_4)\cos\left(\frac{x_1}{\Im(l_2)}\right) - \Im(\alpha_4)\sin\left(\frac{x_1}{\Im(l_2)}\right), \tag{46}$$

and has no physical meaning.

Fig. 5 summarises the four cases just described. As discussed, only the sets of material parameters taken in the areas "1" and "3" lead to physically relevant behaviour. The stability requirements initially presented in Fig. 3(a) are also recalled, the hatched area representing the combination of material parameters leading to a convex potential energy density. This convex domain is associated with both exponentially decreasing and aperiodic physically relevant behaviour.

In the following, the solution of the displacement-equation of equilibrium is supposed to have the general form given in Eq. (42) that is vanishing at infinity. Recalling the discussions made in cases 1 and 3, this implies that l_1^2 and l_2^2 or $\Re(l_1)$ and $\Re(l_2)$ are positive.

Successive derivations of $u_1(x_1)$ give the expressions for $\varepsilon_{11}(x_1)$, $\varepsilon_{111}(x_1)$ and $\varepsilon_{1111}(x_1)$. By using the components of the stress tensors as expressed in Eq. (36), the two last boundary conditions of Eq. (30) become

$$\left(A - \bar{c}\right)\varepsilon_{111} - B\,\varepsilon_{1111,1} = 0, \quad B\,\varepsilon_{1111} + \bar{c}\,\varepsilon_{11} = -b_0 \ \text{ at } x_1 = 0. \tag{47}$$

The two unknown constants α_2 and α_4 in the solution given by Eq. (42) then are

$$\alpha_2 = l_0^2\,\frac{l_1^2\left(l_2^2+l_c^2\right)}{l_1\left(l_2^2+l_c^2\right)^2 - l_2\left(l_1^2+l_c^2\right)^2}, \quad \alpha_4 = -\alpha_2\,\frac{l_2^2\left(l_1^2+l_c^2\right)}{l_1^2\left(l_2^2+l_c^2\right)}, \tag{48}$$

with the new characteristic lengths

$$l_c^2 = \frac{\bar{c}}{\lambda+2\mu} = \frac{1}{2}\,\eta\,L_1^2 \tag{49}$$

and

$$l_0^2 = \frac{b_0}{\lambda+2\mu} = \frac{1}{2}\,\eta_0\,L_1^2. \tag{50}$$

These relations clearly show that no surface effect can occur in the absence of initial higher order stress, i.e., when $b_0 = 0$. Indeed, if the modulus b_0 or its associated dimensionless material parameter η_0 related to surface energy vanishes, the characteristic length l_0 and the constants α_2 and α_4 vanish as well leading finally to $u_1(x_1) = 0$. Note that this complete solution of the boundary value problem is valid for both physically relevant Cases 1 and 3.

The corresponding displacement, strain and stress profiles close to the traction-free surface are presented in Fig. 6. These profiles are obtained for $L_1 = 0.3$ nm, a fixed ratio $L_2^2/L_1^2 = 1$, $\eta_0 = 0.1$ and for four different values of η. These sets of material parameters correspond to the first three cases simulated by the theory: $\eta = -3.0$ and $\eta = -1.2$ belong to the area "1" in Fig. 5 and to u_1 hyperbolic as in Eq. (43); note that $\eta = -3.0$ is not in the convex domain. In the same way, $\eta = 1.3$ and $\eta = 1.9$ belong to areas "2" and "3" and to u_1 as in Eqs. (44) and (45), respectively. The profiles presented in Fig. 6 show that the surface energy effects produced by the theory can either lead to higher or smaller inter-atomic distances close to the free surface. The free surface and subsurface material can therefore be either in tension or compression. Different possible stress distributions are represented in Fig. 6(c), together with a schematic representation of the corresponding atomic positions close to the surface. The results obtained with these parameters are physically relevant, except for $\eta = 1.9$, taken in area "2", which leads to a spurious oscillating solution. It is remarkable that, within the second strain gradient theory with an initial

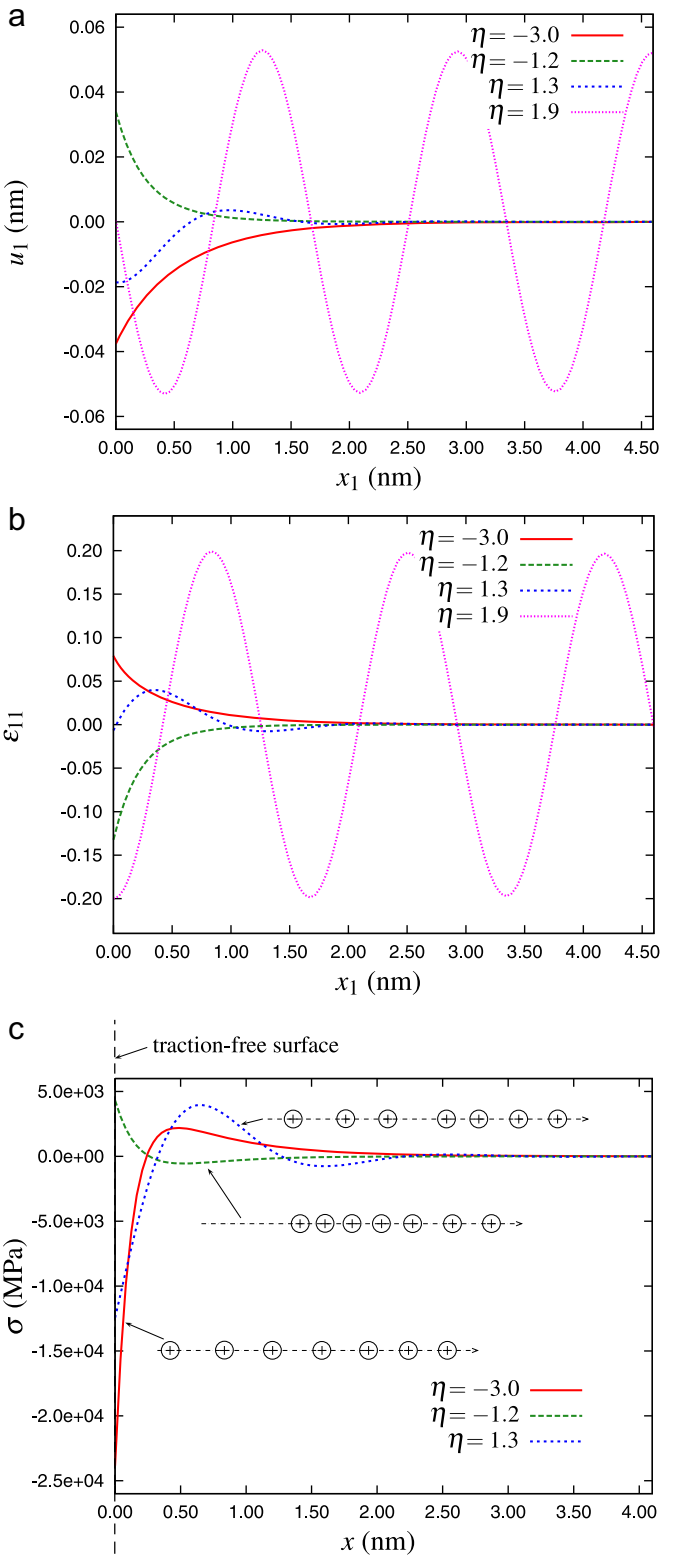

Fig. 6. Profiles of (a) the displacement component u_1, (b) the strain component ε_{11} and (c) the stress component σ_{11} close to the traction-free surface (at $x_1 = 0$). Four sets of material parameters are considered: $E = 140$ GPa, $\nu = 0.3$, $L_1 = 0.3$ nm and a fixed ratio $L_2^2/L_1^2 = 1$. The surface energy related parameter $\eta_0 = 0.1$ and four values of η are used in order to illustrate the four different cases arising in the theory.

cohesion higher order stress, the traction free condition does not lead to a vanishing σ_{11}, as could be expected from Eq. $(30)_1$.

In this configuration, the expression of the surface energy (26) at the planar traction-free surface of the half-space becomes

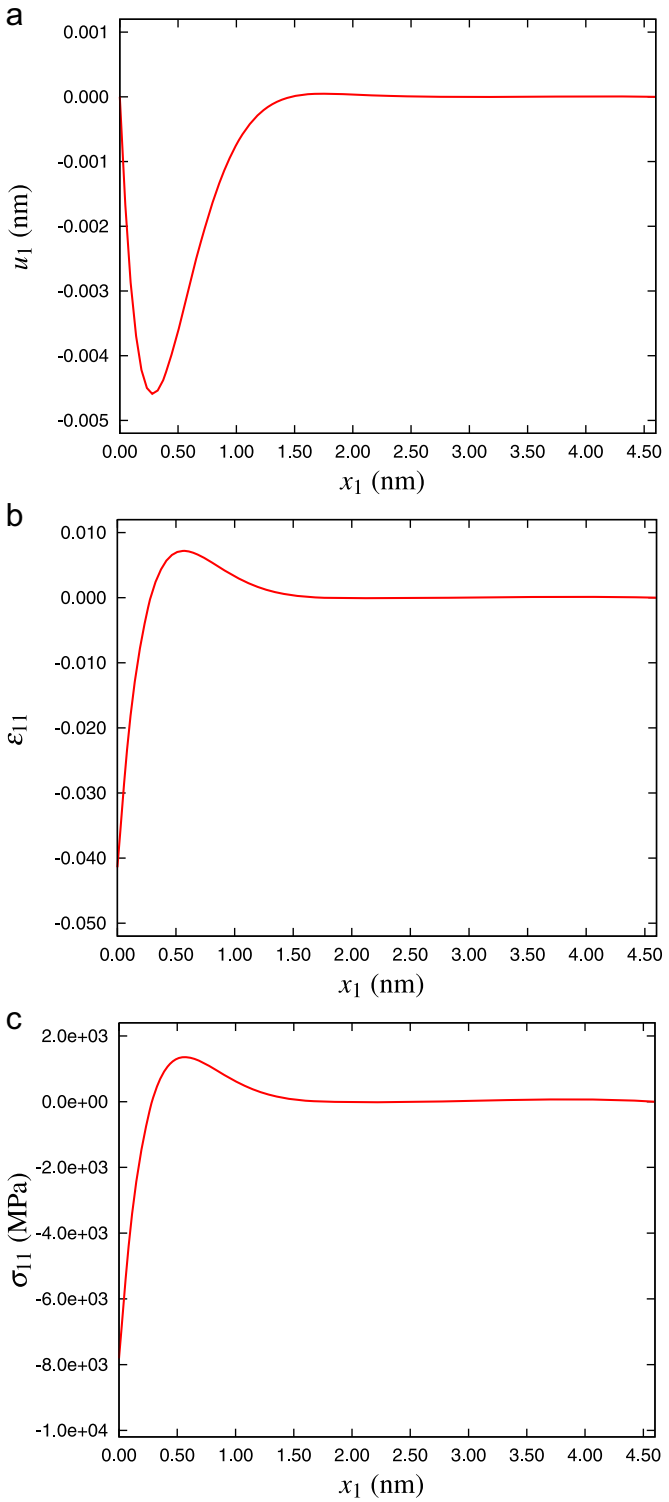

Fig. 7. Profiles of (a) the displacement component u_1, (b) the strain component ε_{11} and (c) the stress component σ_{11} close to the traction-free surface (at $x_1 = 0$). $E = 140$ GPa, $\nu = 0.3$, $L_1 = 0.3$ nm and a fixed ratio $L_2^2/L_1^2 = 1$ are chosen, together with the surface energy related parameter $\eta_0 = 0.1$ and the coupling parameter $\eta = 0$, i.e., $\bar{c} = 0$.

$$\gamma = -\frac{1}{2}b_0\,\varepsilon_{111} = -\frac{1}{2}b_0\left(\frac{\alpha_2}{l_1^2}+\frac{\alpha_4}{l_2^2}\right) = \frac{1}{2}\,\frac{l_0^4\left(\lambda+2\mu\right)\left(l_1^2-l_2^2\right)}{l_1\left(l_2^2+l_c^2\right)^2 - l_2\left(l_1^2+l_c^2\right)^2} \quad \text{at } x_1 = 0. \tag{51}$$

The initial higher order stress, b_0 (or alternatively the corresponding dimensionless material parameter, η_0), only appears in the constants α_2 and α_4 (48) through the characteristic length, l_0^2, then it has no effect on the shape of the simulated behaviour. However, as suggested by Eq. (51), b_0 controls the amplitude of the surface energy.

The effect of the modulus $\bar{c}$ that enables, in the present case, the coupling between the strain, ε_{11}, and the third gradient of the displacement field, ε_{1111}, is presented and discussed in detail in Section 4. At this point, a first remark can be made from the solution of the displacement-equation of equilibrium (42), the expressions of the constants (48) and the expression of $l_c^2 = \bar{c}/(\lambda+2\mu)$. When $\bar{c} = 0$, there is no displacement of the traction-free surface and no volume variation even with a non-zero initial higher order stress, b_0, i.e., $u_1(0) = 0,\ \forall\, b_0$. However, displacements of internal material points occur close to the traction-free surface, i.e., $u_1(x_1 > 0) \neq 0$. This specific case is described in Fig. 7.

3.2. Interaction between two parallel free surfaces

A material strip located at $[-h/2,\ h/2]$ and infinite along the lateral directions 2 and 3 is considered, as described in Fig. 2. Both surfaces at $x_1 = \pm h/2$ are assumed to be traction-free:

$$\underline{\overset{1}{t}} = \underline{\overset{2}{t}} = \underline{\overset{3}{t}} = 0 \quad \text{at } x_1 = \pm\frac{h}{2}, \tag{52}$$

with h being the plate thickness. The purpose here is to show the interaction of the free surface effects evidenced in the previous section when the plate becomes very thin. The conditions $u_2 = u_3 = 0$ are still enforced so that the problem remains one-dimensional. The same resolution steps as in Section 3.1 are then followed so that Eqs. (28)–(40) remain valid and lead to a displacement of the same form as in Eq. (41). The two last boundary conditions in Eqs. (30) and (52) now

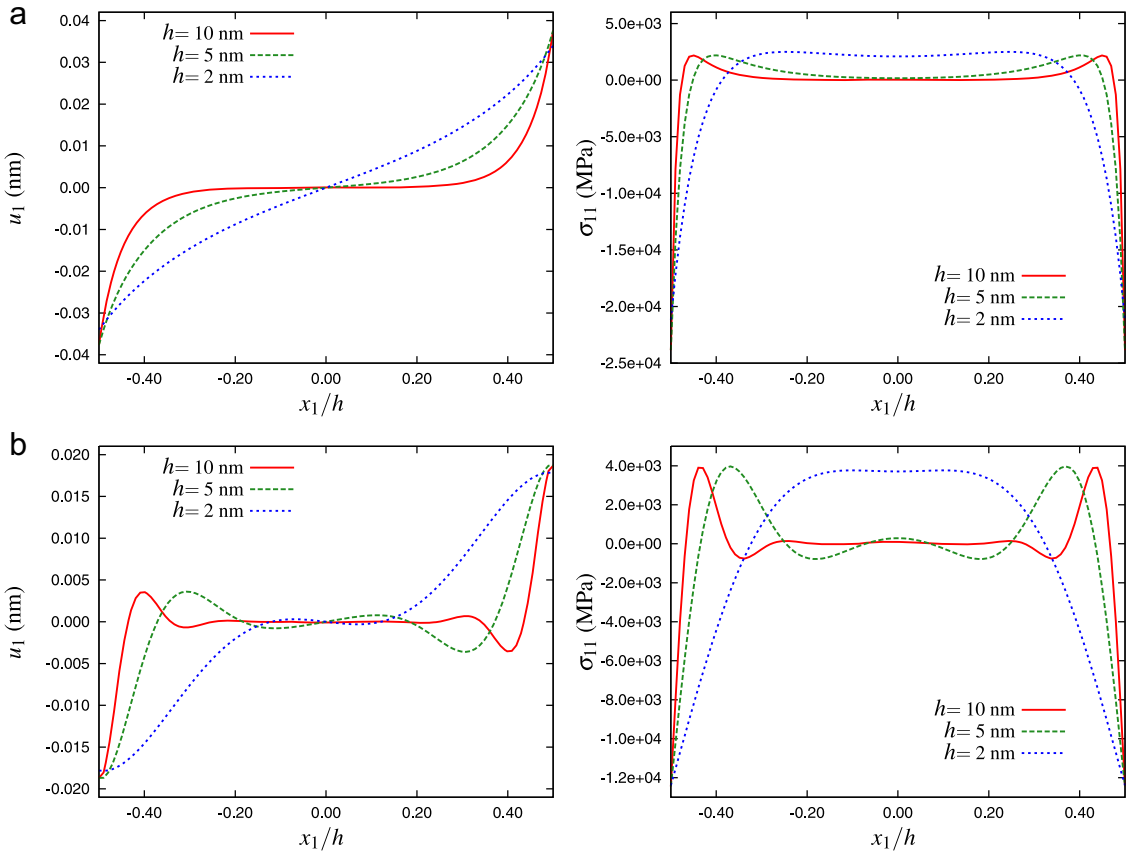

Fig. 8. Profiles of the displacement component u_1 and of stress component σ_{11} for distances between the two traction-free surfaces h=10, 5 and 2 nm and for material parameters leading to (a) exponential (E = 140 GPa, ν = 0.3, L_1 = 0.3 nm, $L_2^2/L_1^2 = 1$, η_0 = 0.1 and $\eta = -3$) and to (b) aperiodic profiles (E = 140 GPa, ν = 0.3, L_1 = 0.3 nm, $L_2^2/L_1^2 = 1$, η_0 = 0.1 and η = 1.3). The free surfaces are located at $x_1/l = \pm 0.5$.

become

$$\left(A-\bar{c}\right)\varepsilon_{111}-B\,\varepsilon_{1111,1}=0,\quad B\,\varepsilon_{1111}+\bar{c}\,\varepsilon_{11}=-b_0\ \text{ at } x_1=\pm\frac{h}{2}. \tag{53}$$

Eqs. (53) are used to determine the constants α_1 to α_6 of the solution (41):

$$\alpha_1=-\frac{1}{2}\,l_0^2\,l_1^2\left(l_2^2+l_c^2\right)\left\{\sinh\left(\frac{h}{2l_1}\right)\left[l_1\left(l_2^2+l_c^2\right]^2\coth\left(\frac{h}{2l_1}\right)-l_2\left(l_1^2+l_c^2\right)^2\coth\left(\frac{h}{2l_2}\right)\right)\right\}^{-1}, \tag{54a}$$

$$\alpha_2=-\alpha_1, \tag{54b}$$

$$\alpha_3=-\alpha_1\,l_2^2\left(l_1^2+l_c^2\right)\sinh\left(\frac{h}{2l_1}\right)\left[l_1^2\left(l_2^2+l_c^2\right)\sinh\left(\frac{h}{2l_2}\right)\right]^{-1}, \tag{54c}$$

$$\alpha_4=-\alpha_3, \tag{54d}$$

$$\alpha_5=0,\quad \alpha_6=0. \tag{54e}$$

If h is large compared to l_1 and l_2, these solutions converge towards the superposition of those solutions for two half-spaces with free surfaces. When h decreases, the perturbations induced by the free surface effect overlap as illustrated next. The profiles of the displacement component u_1 and stress component σ_{11} are presented in Fig. 8 for different distances h and for sets of material parameters giving hyperbolic and aperiodic solutions, as discussed in Section 3.1.

The used sets of parameters systematically lead to a thickening of the plate induced by the surface energy effect since $u_1(h/2)>0$, $u_1(-h/2)<0$ in all figures. The shrinking or thickening of the plate is directly related to the sign of b_0 via the parameter η_0 in l_0^2, cf. Eq. (50) and (33). Very large σ_{11} stress values, sometimes exceeding 10 GPa, are found at the free surfaces. For larger values of h, e.g., $h=10$ nm, the profiles close to the free surfaces are the same as in the half-space case, see Fig. 6. When h becomes smaller, the zones affected by the surface energy effects start to overlap and the resulting profiles are significantly modified. In particular, the strain, ε_{11}, becomes almost homogeneous for very thin plates whereas it is localised close to the free surface for thicker samples. This case appears to be of great interest as it is encountered in nano-sized objects such as nano-wires or nano-porous materials where surfaces are very close to each other.

4. Surface elasticity effect: apparent shear of an infinite strip

Casal (1961, 1963) was the first to theoretically consider the tension of a nano-wire made of an isotropic first strain gradient material. He derived the boundary layers' effects at the ends of a beam induced by higher order boundary conditions. However, he did not mention the non-homogeneous straining close to a free surface. This is due to the fact that such effects cannot arise in isotropic first strain gradient materials. These phenomena akin to surface elasticity are now illustrated for the second strain gradient continuum.

The purpose of this section is to show how the theory can describe surface effects induced by the coupling between the strain, $\underline{\underline{\varepsilon}}$, and the third gradient of the displacement field, $\underline{\underline{\underline{\underline{\varepsilon}}}}$. This coupling is controlled by the moduli c_i, as can be seen from the constitutive equations (24a) and (24c).

The tension of nano-wires and their apparent elastic properties will be investigated based on finite element simulations to be presented in Section 5.1. In this section, the notion of apparent elastic property is defined in the context of third gradient elasticity. Analytical expressions for the apparent shear modulus are derived for an infinite thin strip subjected to shear.

4.1. Resolution of the boundary value problem

The simple shear of an infinite strip of thickness h is considered as described in Fig. 9. Displacements are prescribed to the upper and lower surfaces corresponding to simple shear:

$$u_1(h/2)=\frac{U_0}{2},\quad u_1(-h/2)=-\frac{U_0}{2}. \tag{55}$$

These upper and lower surfaces are assumed to be free of higher order tractions, i.e.,

$$\underline{\underline{\underline{t}}}^{2}=\underline{\underline{\underline{t}}}^{3}=0\quad \text{at } x_2=\pm\frac{h}{2}, \tag{56}$$

In addition, in order to focus exclusively on the surface elasticity effects, no surface energy is considered. In other words, the

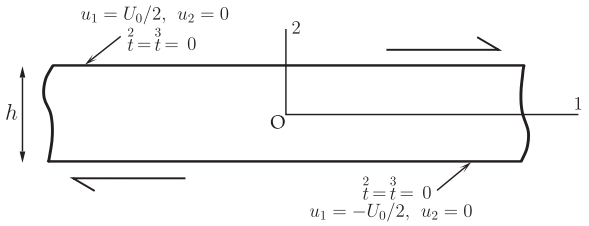

Fig. 9. Shear of an infinite strip of thickness h. Dirichlet displacement conditions are applied to the upper and lower surfaces. These surfaces are free of higher order tractions.

initial higher order stress, b_0, related to surface energy is taken to be equal to zero. Due to the infinite lateral extension of the strip, the displacement field takes the form

$$u_1 = u_1(x_2), \quad u_2 = u_3 = 0. \tag{57}$$

The stress balance equation (21) becomes

$$\sigma_{12,2} - S_{122,22} + S_{1222,222} = 0 \tag{58}$$

and the two last boundary conditions (22) are

$$S_{122} - S_{1222,2} = S_{1222} = 0 \quad \text{at } x_2 = \pm \frac{h}{2}. \tag{59}$$

Recalling the displacement field (57), then the strain energy density (23) is a function of the strain components ε_{12}, ε_{122} and ε_{1222}:

$$\rho\Psi\Big(\varepsilon_{12},\ \varepsilon_{122},\ \varepsilon_{1222}\Big) = \mu\,\varepsilon_{12}^2 + \frac{A}{2}\,\varepsilon_{122}^2 + \frac{B}{2}\,\varepsilon_{1222}^2 + c_3\,\varepsilon_{12}\,\varepsilon_{1222} \tag{60}$$

with the new definitions of reduced moduli A and B superseding (32),

$$A = 2(a_3 + a_4), \quad B = 2(b_5 + b_6). \tag{61}$$

In the same way as in Sections 3.1 and 3.2, the following reduced material parameters are introduced:

$$L_1^2 = \frac{A}{\mu}, \quad L_2^2 = \frac{B}{A}, \quad \eta = \frac{c_3}{A}, \tag{62}$$

which are used to express the potential energy density (60) as a function of dimensionless arguments:

$$\rho\Psi\Big(\varepsilon_{12},\ \varepsilon_{122},\ \varepsilon_{1222}\Big) = \rho\hat{\Psi}\Big(\varepsilon_{12},\ L_1\,\varepsilon_{122},\ L_2^2\,\varepsilon_{1222}\Big). \tag{63}$$

The following requirements can then be obtained based on the convexity of the strain energy potential,

$$L_1^2 \geq 0, \quad L_2^2 \geq 0, \quad 2\,\frac{L_2^2}{L_1^2} \geq \eta^2. \tag{64}$$

This implies that the moduli A and B must be positive while c_3 can be either positive or negative. The components σ_{12}, S_{122} and S_{1222} of the stress tensors are obtained from Eqs. (60), (10) and (24):

$$\sigma_{12} = 2\mu\,\varepsilon_{12} + c_3\,\varepsilon_{1222}, \tag{65a}$$

$$S_{122} = A\,\varepsilon_{122}, \tag{65b}$$

$$S_{1222} = B\,\varepsilon_{1222} + c_3\,\varepsilon_{12}. \tag{65c}$$

Substituting these expressions into the stress-equation of equilibrium (58) and recalling that $\varepsilon_{12} = 1/2\,u_{1,2}$, $\varepsilon_{122} = 1/2\,u_{1,22}$ and $\varepsilon_{1222} = 1/2\,u_{1,222}$, the following displacement-equation for equilibrium is obtained:

$$\left(1 - l_1^2\,\frac{d^2}{dx_2^2}\right)\left(1 - l_2^2\,\frac{d^2}{dx_2^2}\right)\frac{d^2u_1}{dx_2^2} = 0. \tag{66}$$

The relationships,

$$l_1^2 l_2^2 = \frac{B}{2\mu}, \quad l_1^2 + l_2^2 = \frac{A - 2c_3}{2\mu}, \tag{67}$$

are derived and lead to the following expressions for the lengths l_1 and l_2:

$$l_1^2 = \frac{A - 2c_3 + \sqrt{(A - 2c_3)^2 - 8B\mu}}{4\mu}, \quad l_2^2 = \frac{A - 2c_3 - \sqrt{(A - 2c_3)^2 - 8B\mu}}{4\mu}, \tag{68}$$

or alternatively:

$$l_1^2 = \frac{L_1^2}{4}\left(1 - 2\eta + \sqrt{(1 - 2\eta)^2 - 8\frac{L_2^2}{L_1^2}}\right), \quad l_2^2 = \frac{L_1^2}{4}\left(1 - 2\eta - \sqrt{(1 - 2\eta)^2 - 8\frac{L_2^2}{L_1^2}}\right). \tag{69}$$

It can be noted that the chosen notations for the material parameters L_1, L_2 and η lead to the same expressions of the stability requirements (35) and of the characteristic lengths (40) as in Sections 3.1 and 3.2.

The solution of Eq. (66) takes the form

$$u_1(x_2) = \alpha_1\, e^{x_2/l_1} + \alpha_2\, e^{-x_2/l_1} + \alpha_3\, e^{x_2/l_2} + \alpha_4\, e^{-x_2/l_2} + \alpha_5\, x_2 + \alpha_6, \tag{70}$$

and the boundary conditions (59) require that

$$\left(A - c_3\right)\varepsilon_{122} - B\,\varepsilon_{1222,2} = 0, \quad B\,\varepsilon_{1222} + c_3\,\varepsilon_{12} = 0 \ \text{ at } x_2 = \pm\frac{h}{2}, \tag{71}$$

They are used to find the expressions of the constants α_1 to α_6:

$$\alpha_1 = U_0\, l_c^2\, l_1^2\left(l_2^2 + l_c^2\right)\left\{\sinh\left(\frac{h}{2l_1}\right)\left[4\, l_c^4\left(l_1^2 - l_2^2\right) - 2h\left(l_1\left(l_2^2 + l_c^2\right)^2 \coth\left(\frac{h}{2l_1}\right)\right.\right.\right.$$
$$\left.\left.\left. - l_2\left(l_1^2 + l_c^2\right)^2 \coth\left(\frac{h}{2l_2}\right)\right)\right]\right\}^{-1}, \tag{72a}$$

$$\alpha_2 = -\alpha_1, \tag{72b}$$

$$\alpha_3 = -\alpha_1\, l_2^2\left(l_1^2 + l_c^2\right)\sinh\left(\frac{h}{2l_1}\right)\left[l_1^2\left(l_2^2 + l_c^2\right)\sinh\left(\frac{h}{2l_2}\right)\right]^{-1}, \tag{72c}$$

$$\alpha_4 = -\alpha_3, \tag{72d}$$

$$\alpha_5 = -2\alpha_1\, \sinh\left(\frac{h}{2l_1}\right)\left[l_1\left(l_2^2 + l_c^2\right)^2 \coth\left(\frac{h}{2l_1}\right) - l_2\left(l_1^2 + l_c^2\right)^2 \coth\left(\frac{h}{2l_2}\right)\right]\left[l_c^2\, l_1^2\left(l_2^2 + l_c^2\right)\right]^{-1}, \tag{72e}$$

$$\alpha_6 = 0, \tag{72f}$$

with the new characteristic length,

$$l_c^2 = \frac{c_3}{2\mu} = \frac{1}{2}\,\eta\, L_1^2. \tag{73}$$

Recall that the initial higher order stress, b_0, and its related characteristic length, l_0^2, do not appear in these expressions as the surface energy is purposely not considered in the present case. Examination of Eqs. (72) shows that surface effects only occur if a coupling exists between the component of the strain ε_{12} and the component of the third gradient of the displacement field ε_{1222}. If the coupling modulus $c_3 = 0$, then $l_c = 0$, $\alpha_1 = \alpha_2 = \alpha_3 = \alpha_4 = 0$ and $\alpha_5 = U_0/h$. The standard homogeneous shear solution is retrieved: $u_1(x_2) = U_0 x_2/h$.

The same remark can be made on the imposed displacement at the upper and lower surfaces. Indeed, if $U_0 = 0$, all the constants α_i in Eq. (70) vanish and then $u_1(x_2) = 0$. This would not be the case in the presence of surface energy since, as shown is Section 3.1, surface and subsurface straining arises even in the absence of external loading at traction-free surfaces.

The profiles of the displacement component u_1 and of stress component σ_{12} are shown in Fig. 10 for various thicknesses h of the strip and for sets of material parameters leading to physically acceptable hyperbolic and aperiodic solutions. This figure shows that for larger thicknesses h of the strip, the profiles are almost linear and close to the solution for a classical continuum. The surface and subsurface elasticity effects are found to be localised at the upper and lower surfaces, and the

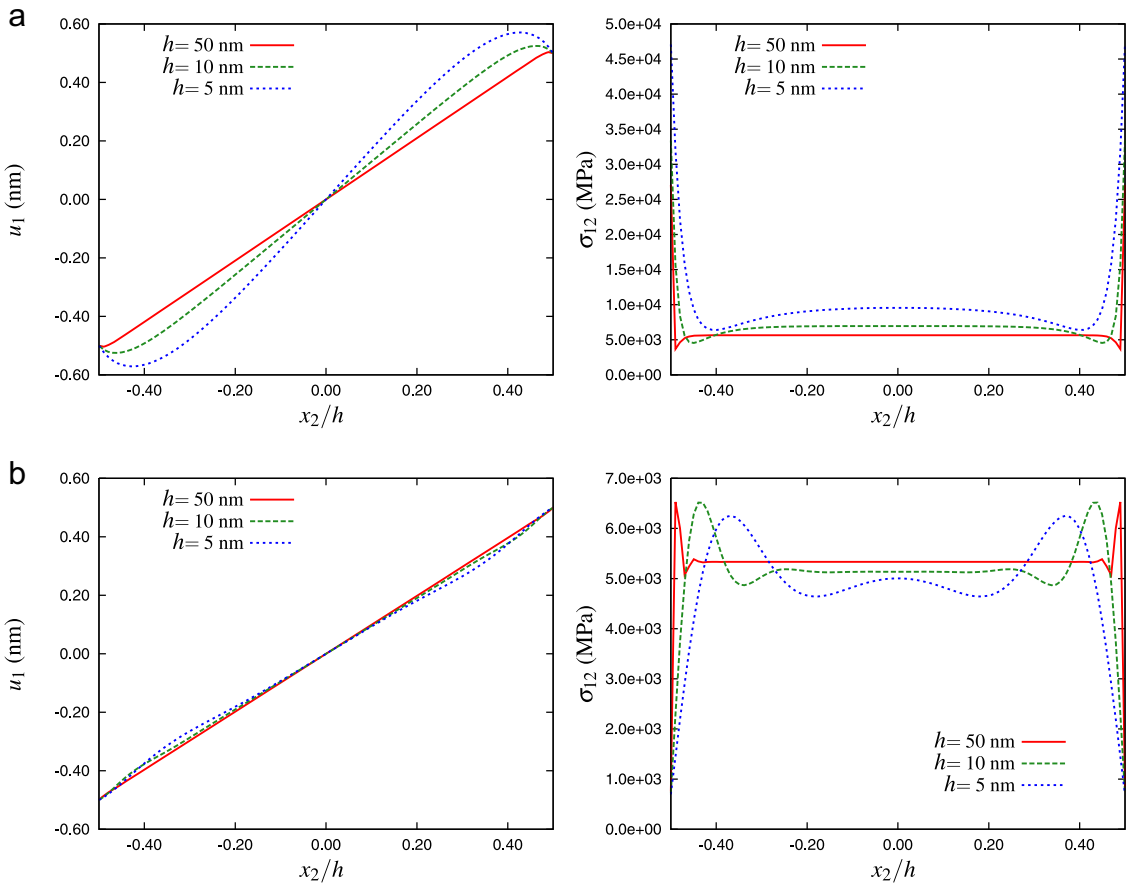

Fig. 10. Profiles of the displacement component u_1 and of stress component σ_{12} for thicknesses of the infinite strip, $h=50$, 10 and 5 nm, and for material parameters leading to (a) exponential ($E = 140$ GPa, $\nu = 0.3$, $L_1 = 0.3$ nm, $L_2^2/L_1^2 = 1$ and $\eta = -3$) and to (b) aperiodic profiles ($E = 140$ GPa, $\nu = 0.3$, $L_1 = 0.3$ nm, $L_2^2/L_1^2 = 1$ and $\eta = 1.3$). In both cases, the surface energy is not considered, i.e., $b_0 = \eta_0 = 0$.

affected zones remain small compared to the thickness h. These surface effects become stronger when the strip gets thinner, i.e., when the higher order traction-free surfaces get closer to each other.

4.2. Determination of the apparent shear modulus

Experimental measurements of apparent elastic properties of nano-objects are based on the ratio of effective stress and strain properties, since the direct measurement of higher order stresses remains an open question. Such apparent quantities can be derived from the previous theory by proper averaging procedures.

The apparent shear modulus μ^{app} is defined by averaging the stress component, σ_{12}, and the strain component, ε_{12}, along the thickness of the infinite strip as

$$\int_{-h/2}^{h/2} \sigma_{12}\, dx_2 = 2\,\mu^{app} \int_{-h/2}^{h/2} \varepsilon_{12}\, dx_2. \tag{74}$$

The following expression of the apparent shear modulus is then obtained from the analytical solution of Section 4.1:

$$\mu^{app} = \mu\, \frac{l_1\left(l_2^2 + l_c^2\right)^2 \coth\left(\frac{h}{2l_1}\right) - l_2\left(l_1^2 + l_c^2\right)^2 \coth\left(\frac{h}{2l_2}\right)}{l_1\left(l_2^2 + l_c^2\right)^2 \coth\left(\frac{h}{2l_1}\right) - l_2\left(l_1^2 + l_c^2\right)^2 \coth\left(\frac{h}{2l_2}\right) - \frac{2}{h}\, l_c^4\left(l_1^2 - l_2^2\right)}. \tag{75}$$

or, equivalently,

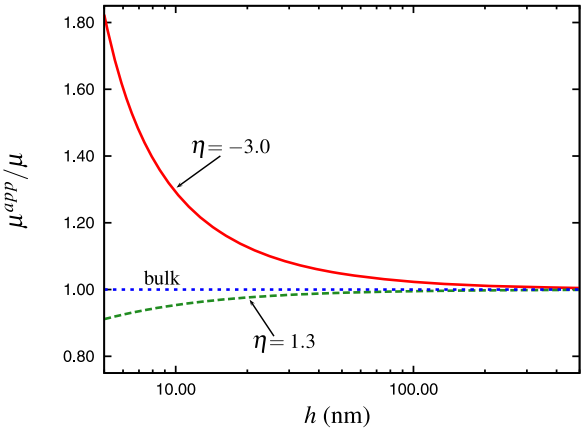

Fig. 11. Effect of the thickness of the infinite strip, h, on the evolution of the apparent shear modulus, μ^{app}, for $E = 140$ GPa, $\nu = 0.3$, $L_1 = 0.3$ nm, $L_2^2/L_1^2 = 1$ and for two different values of the coupling parameter, η. The horizontal line corresponds to the classical solution obtained without coupling ($\eta = 0$), or equivalently, without surface stress effects. Note that in all of these cases, the surface energy is not considered, i.e., $b_0 = \eta_0 = 0$.

$$\frac{\mu}{\mu^{app}} = 1 - \frac{2}{h}\frac{l_c^4\left(l_1^2 - l_2^2\right)}{l_1\left(l_2^2 + l_c^2\right)^2 \coth\left(\frac{h}{2l_1}\right) - l_2\left(l_1^2 + l_c^2\right)^2 \coth\left(\frac{h}{2l_2}\right)}. \tag{76}$$

It is apparent in this relation that μ^{app} is size-dependent, the effect of the thickness h on its value is plotted for different sets of material parameters in Fig. 11. For large values of h, the surface elasticity effects are negligible and the bulk shear modulus μ is retrieved,

$$\lim_{h\to\infty} \mu^{app} = \mu. \tag{77}$$

When the strip thickness decreases, the apparent elastic property progressively departs from one of the bulk and tends to the limit

$$\lim_{h\to 0} \mu^{app} = \mu\left(1 - \frac{l_c^4}{l_1^2 l_2^2}\right). \tag{78}$$

Note that when the coupling modulus, c_3, or equivalently the characteristic length, l_c, vanishes, the ratio μ^{app}/μ is equal to one and no surface elasticity effect arises. Fig. 11 shows that the apparent shear modulus, μ^{app}, can either increase or decrease for smaller h. This only depends on the material parameter related to the coupling, namely η controlling the sign of l_1^2 and l_2^2 according to (68). In this figure, the horizontal line corresponds to the classical solution obtained without surface elasticity effects. The same dependency appears in the limit presented in Eq. (78). The positivity of the limit apparent shear modulus given by Eq. (78), and therefore the local stability of the material under shear, is ensured when $l_1^2 l_2^2 - l_c^4 = L_1^2(2L_2^2 - \eta^2 L_1^2)/4 > 0$ which is equivalent to the already stated stability condition (64). When both l_1^2 and l_2^2 are positive the nano-scale apparent shear modulus is lower than the bulk one. The values of l_1^2 and l_2^2 can be of distinct sign, one being positive, the other one negative, for some negative values of η. This situation leads to a stiffening effect at nano-scale as shown in Fig. 11. However, the stability conditions (64) require $l_1^2 l_2^2 = L_1^2 L_2^2/2$ be positive. As a result, shear stiffening cannot occur in the locally stable regime. This statement is however limited to the boundary value problem considered in this section, namely a simple shear test with vanishing higher order tractions at the lower and upper boundaries, see Fig. 9.

Some specific cases can be investigated to fully understand the surface stress effects. For example, if $l_1 = l_2$ (i.e., $(1 - 2\eta)^2 = 8\, L_2^2/L_1^2$), no effect is produced and then

$$\mu^{app}_{(l1=l2)} = \mu. \tag{79}$$

This is the specific case of the double root of the differential equation (66). It corresponds to the parabola of Fig. 3 (b) separating the two domains in which l_1^2 and l_2^2 are real or complex. Moreover, if the generalised modulus related to the second strain gradient, B, vanishes, we have $L_2 \to 0$, $l_2 \to 0$ and finally

$$\lim_{B\to 0} \mu^{app} = \mu\frac{h\ \coth\left(\frac{h}{2l_1}\right)}{h\ \coth\left(\frac{h}{2l_1}\right) - 2l_1}. \tag{80}$$

This means that the theory generates size-dependent surface stress effects even if B vanishes. This confirms the fact that, as mentioned before, the surface stress effects predicted by the second strain gradient theory solely depend on the coupling parameter between the strain component, ε_{12}, and the third gradient of the displacement field component, ε_{1222}.

5. Application to the static elastic behaviour of nano-objects

Now that the capabilities of the theory and, more particularly, the generated surface effects, have been demonstrated, more realistic and complex boundary value problems will be considered. They are performed by means of finite element simulations making use of the constrained generalised micromorphic approach proposed by Germain (1973b), Forest (2009), and Forest et al. (2011).

5.1. Apparent tensile elastic behaviour of second strain gradient nano-films

The size-dependent tensile behaviour of nano-objects, especially nano-wires, has been widely investigated due to their key role in nano-electromechanical systems (NEMS) (Thomas et al., 2011; Craighead, 2000; Feng et al., 2007; Sanii and Ashby, 2010). In particular, their size-dependent elastic properties are studied experimentally using various methods (see, for example, Agrawal et al., 2008; McDowell et al., 2008; Sadeghian et al., 2009). Nano-wires exhibit a very high surface area to volume ratio and therefore their behaviour is strongly affected by surface effects. Using the previous results as a guideline to define the material parameters, the overall behaviour of such nano-objects and especially the local strain fields are studied using finite element simulations. To that purpose, the second gradient of strain theory presented in Section 2 is implemented using the second order micromorphic approach formulated in Appendix A. The micromorphic model is constrained through the moduli H_χ^a and H_χ^b in Eqs. (96) to be as close as possible to the gradient theory. In what follows, H_χ^a and H_χ^b are taken sufficiently high to ensure this internal constraint. The main features of the finite element implementation are given in Appendix B. Isoparametric quadratic elements with reduced integration are used.

The boundary value problem solved by means of the finite element method is depicted in Fig. 12(a). Here, a long plate with thickness, d, is subjected to prescribed displacement $u_2 = U$ at the top in the direction 2 and fixed displacement u_2 at the bottom. Plane strain conditions are enforced, i.e. $u_3 = 0$. Periodicity conditions are imposed to the additional micro-deformation degrees of freedom, between the top and bottom surfaces. The lateral surfaces $x_1 = \pm d/2$ are traction-free at any order, meaning that

$$\underline{\overset{1}{t}} = \underline{\overset{2}{t}} = \underline{\overset{3}{t}} = 0 \quad \text{at } x_1 = \pm \frac{h}{2}, \tag{81}$$

at the vertical sides of the 2D geometry presented in Fig. 12(a). In these conditions, the nano-films can be considered of infinite length and finite width, d.

Tensile tests on thin films with various thicknesses, d, are simulated in that way. In these tests, the nano-objects are assumed to remain elastic. The contour plots of Fig. 12(b) and the corresponding profiles across the thickness in Fig. 12 (c) describe the simulated fields of the lateral strain and axial stress components, ε_{11} and σ_{22}, obtained for three thicknesses and with the material parameters given in Table 2. These parameters are presented using the notation (33) introduced in Section 3 and the corresponding generalised moduli A, B, c_i and b_0 are also given. The coupling moduli c_i' used in the micromorphic model are defined using the equivalences between c_i and c_i', see Eq. (108). The results given in Fig. 12 reveal that the surface stress effects are localised at the surface of the larger film of thickness $d = 50$ nm. The fields and profiles of ε_{11} and σ_{22} are then close to those that can be obtained with a classical continuum. However, for smaller d, the surface stress effects become more significant and the affected zone spreads across the thickness. These results agree with the previous observations made in the infinite strip shear case.

Recalling that plane strain conditions are used, the apparent Poisson ratio, ν^{app}, and the apparent Young modulus, E^{app}, are calculated as

$$\nu^{app} = \frac{\varepsilon_{11}}{\varepsilon_{11} - \varepsilon_{22}} \tag{82}$$

and

$$E^{app} = \frac{\sigma_{22}(1 - \nu^{app2})}{\varepsilon_{22}}, \tag{83}$$

where the macroscopic strains and stress ε_{11}, ε_{22} and σ_{22} are computed from the finite element simulations by averaging the corresponding quantities over the whole sample. These apparent elastic constants are found to be size-dependent. Fig. 13 shows the effect of the film thickness, d, on the evolution of the apparent Young modulus, E^{app}, for the material parameters given in Table 2. These parameters were identified in order to reproduce, as quantitatively as possible, the size-dependent behaviour of ZnO nano-wires for which experimental data is available (Agrawal et al., 2008). In the experiment, tensile tests were performed on single crystal ZnO nano-wires having a [0001] oriented wurtzite structure. It must be noted that the real

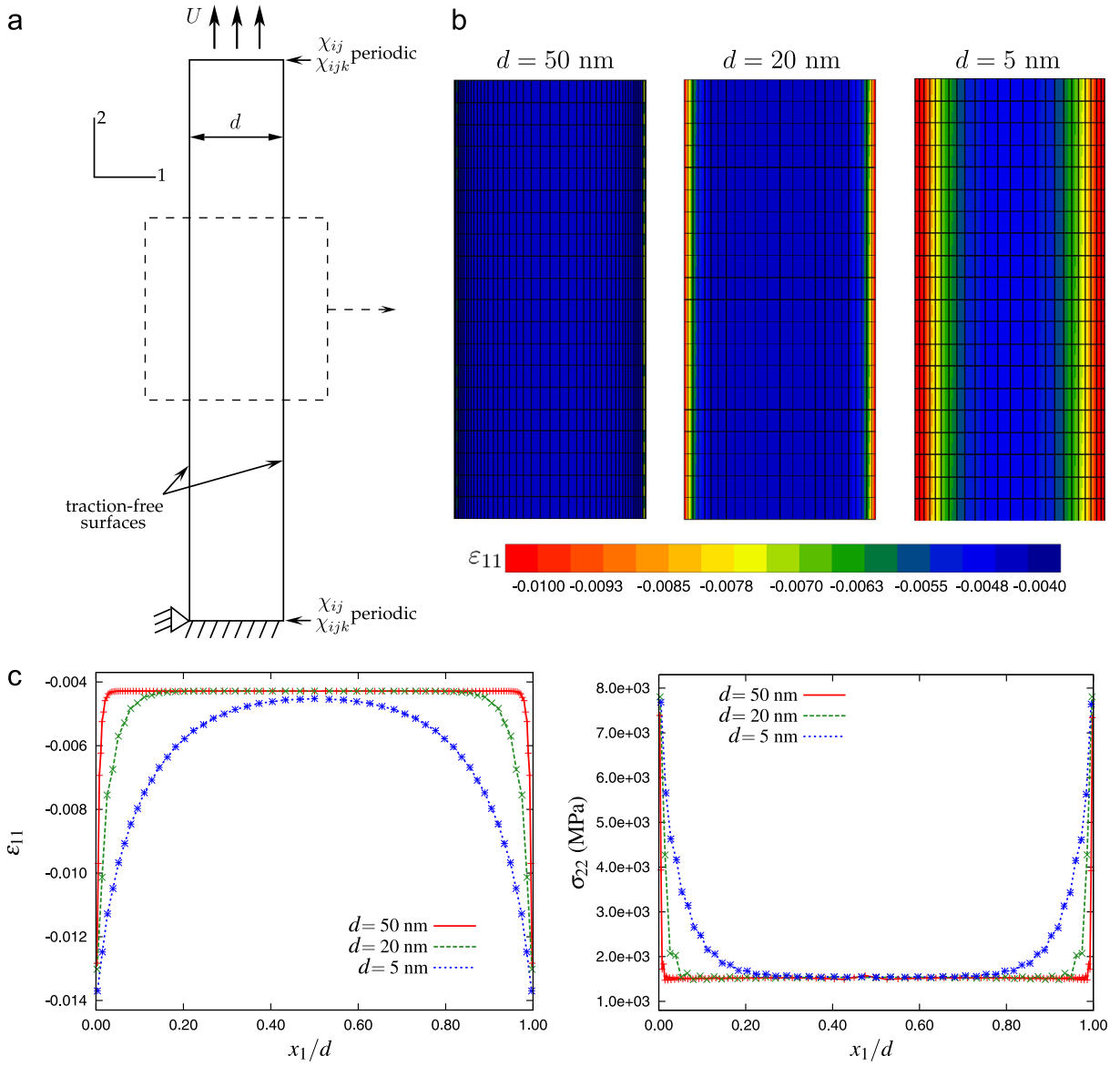

Fig. 12. Finite element simulations of tensile tests of thin films with material parameters given in Table 2. (a) Description of the boundary value problem, (b) contour plots of the strain component ε_{11} and (c) profiles of the strain and stress components, ε_{11} and σ_{22}, across the film's thickness.

Table 2
Set of material parameters used in the finite element simulations, and the corresponding characteristic lengths and dimensionless parameters.

E (GPa)	ν	A (N)	B (N nm^2)	c_1 (N)	$c_{i\neq 1}$ (N)	b_0 (N)
140	0.3	9.4×10^{-8}	4.7×10^{-8}	-2.8×10^{-7}	0	0

E (GPa)	ν	L_1 (nm)	L_2^2/L_1^2	η	η_0
140	0.3	1.0	0.5	−3	0

single crystal exhibits anisotropic elastic and surface properties whereas our work concentrates on isotropic second strain gradient elasticity. Accordingly, the performed identification is valid only in the [0001] direction and considerable additional theoretical and experimental work is needed to extend the approach to the fully anisotropic case. Besides, fitting the

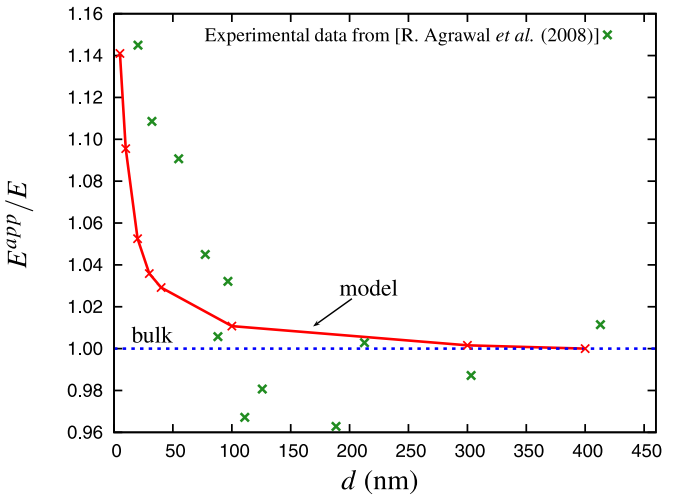

Fig. 13. Effect of the nano-film thickness, d, on the evolution of the apparent Young modulus, E^{app}, for the material parameters given in Table 2. The horizontal line corresponds to the classical solution obtained without surface effects or equivalently to the bulk Young modulus. The plotted experimental data come from Agrawal et al. (2008) and are obtained with tensile tests of single crystal ZnO nano-wires having a [0001] oriented wurtzite structure.

simulation results for nano-plates to the experimental results for nano-wires can only lead to tentative and qualitative values of the corresponding moduli. The identification was performed using the results from the previous sections as a guideline. Indeed, the value of the material parameter related to the coupling is first set at $\eta = -3$ because it provides a realistic order of magnitude of surface displacement but, unfortunately no experimental information is available for the apparent Poisson ratio. Then, the only dimensional parameter, L_1, is calibrated to obtain a size dependent zone for a range of thicknesses that correspond to the experimental results. Finally, the ratio L_2/L_1 is calibrated to refine the fitting. The identified material parameters are of the same order of magnitude as those used in the simple cases treated earlier in this paper. The experimental results are far too scattered and not numerous enough to identify a unique set of material parameters. The chosen parameters provide sensible results, though probably exaggerated since the actual size effects may arise at smaller length scales than 100 nm predicted by the model in Fig. 13. A more accurate identification is possible by means of molecular dynamics or ab initio simulations. However, large uncertainties remain also with this method because the confidence on higher order moduli predicted by such discrete methods is necessarily very limited.

It turns out that the chosen material parameters η, L_1, L_2 fall in the non-convex domain delimited in Section 3. Although no complete identification of the material parameters was possible due to the limited amount of information available for ZnO, the exploration of the parameter space lead us to non-positive definite higher order moduli to reproduce the qualitative increase of the apparent Young modulus for nano-sizes. This finding should be related to the identification of negative first strain gradient higher order elastic moduli sometimes found by comparison with the results of atomistic simulations, see Maranganti and Sharma (2007). Negative surface elasticity properties were also found in the context of bulk conventional elasticity with energetic and elastic surfaces, see Yvonnet et al. (2008). This question is discussed by Javili et al. (2012) who show mesh dependent finite element simulation results when using negative surface elasticity with a bulk stable elastic substrate. The relevance of the proposed parameters and the possible need for higher order regularisation remain open questions which require a thorough analysis of the well-posedness of the associated variational problem.

In the same way, Fig. 14 shows the effect of d on the evolution of the apparent Poisson ratio, ν^{app}. A strong enhancement of the apparent Poisson ratio is found for thicknesses less than 20 nm. It is remarkable that the apparent Poisson ratio is found to tend toward 0.5 in the performed simulations for vanishingly small thicknesses.

The second gradient of strain theory presented in Section 2 is thus able to account, at least qualitatively, for the size-dependent elastic properties of nano-objects. Their mechanical behaviour is affected by surface effects that occur in a surface region of a few nanometers. The obtained results show that these surface effects can be neglected when the thickness is equal to some tens of nanometers or larger. For such sizes, the elastic properties of the bulk material are retrieved.

5.2. *Free surface effects in periodic porous nano-structures*

Nano-porous materials arouse a strong interest for catalysis and the storage of hydrogen or CO_2 wastes due to their outstanding surface to volume ratio (Thomas et al., 2011). The surface effect induced by surface energy and surface elasticity can have a strong impact on the macroscopic behaviour depending on the void volume fraction. Effective mechanical properties can be determined based on generalised homogenisation methods. For instance, the effective first displacement gradient theory was identified from the atomic potentials for nano-porous silicon by Magoariec and Danescu (2009). Lattice

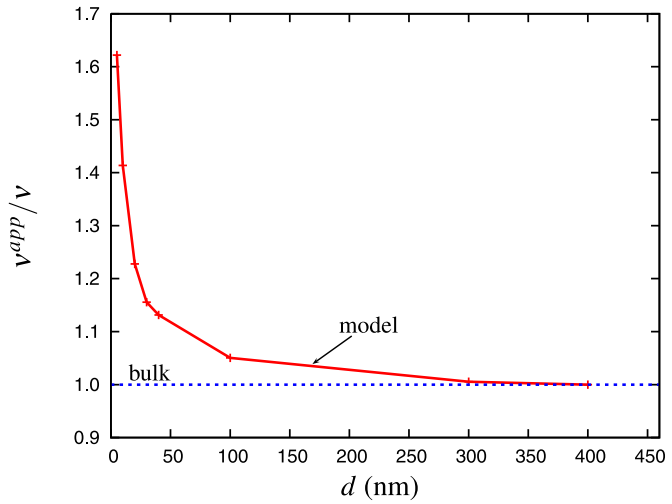

Fig. 14. Effect of the nano-film thickness, d, on the evolution of the apparent Poisson's ratio, ν^{app}, for the material parameters given in Table 2. The horizontal line corresponds to the classical solution obtained without surface effects.

dynamics was used by Danescu and Grenet (2012) for the determination of first strain gradient elastic moduli. Danescu (2012) shows the drawbacks of the first strain gradient model and recommends, instead, the use of the so-called hyper-prestress, associated with size-dependent lattice parameter. This model was applied to surface relaxation of nano-porous silicon. The isotropic second strain gradient theory is an alternative to model this effect.

The problem of surface relaxation in a periodic nano-porous material is now studied by means of the second strain gradient theory and the finite element method. For that purpose, a hexagonal array of holes embedded in a matrix under plane strain conditions is considered. The initial unit cell is shown in Fig. 15 (left). Periodic boundary conditions are applied at the boundary of the hexagonal cell. The inner surface of the hole is traction-free. An initial hole diameter of 5 nm is considered. The size of the hexagonal unit cell corresponds to a porosity of 0.3. The objective of the computation is to determine the relaxed shape of the hole induced by the presence of the cohesive initial higher order stress b_0. No external loading is applied. The material parameters used in the simulation are

$$c_1 = -10^{-8}\ \text{N}, \quad c_{i\neq 1} = 0, \quad A = 10^{-8}\ \text{N}, \quad B = 10^{-9}\ \text{N nm}^2, \quad b_0 = 10^{-9}\ \text{N}$$

corresponding to

$$\eta = \frac{\bar{c}}{A} = -1, \quad \eta_0 = \frac{b_0}{A} = 0.1$$

The previous parameters A and B refer to the higher order elasticity moduli defined by Eq. (97) in Appendix A.

The release of tractions at the hole surface is shown in Fig. 15 (right) to result in the deformation of the hole and the subsurface. With a chosen positive sign of b_0, the hole is found to shrink by about 2%, most of the strain taking place in the

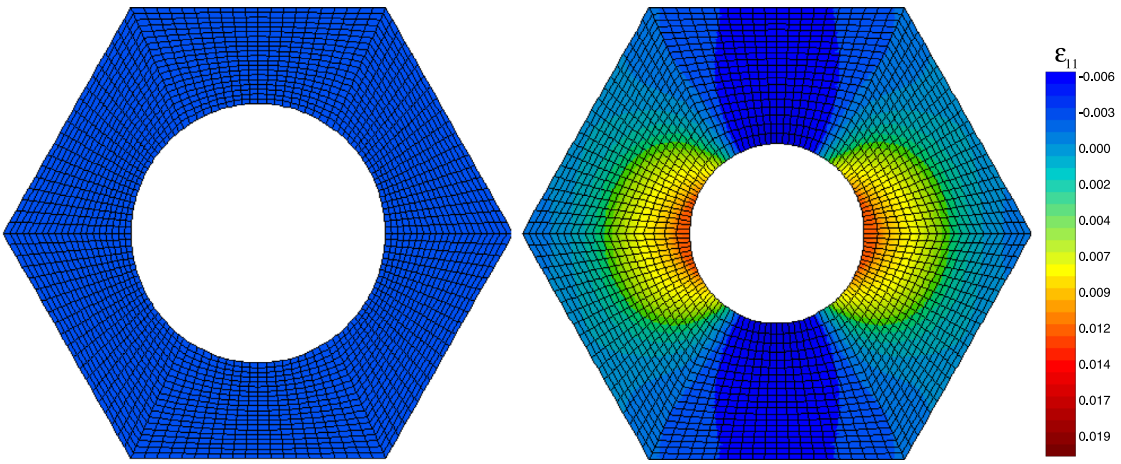

Fig. 15. Unit cell of a periodic nano-porous material: initial configuration (left), deformed state (right, deformation magnified by 1000) and field of the Cartesian strain component ε_{11}, the direction 1 denoting the horizontal direction.

first row of elements around the hole. In the periodic system, holes are close enough for the strained regions around the hole to overlap. This kind of computation can be used to identify the value of the material parameter b_0 from the measured distribution of hole size changes and lattice distortion around holes in nano-porous materials. Note that such measurements are rendered more difficult by the fact that the surface of nano-porous materials generally is contaminated by external chemical elements like hydrogen, especially in the case of percolating nano-porosity and hydrogen storage in such materials.

6. Conclusions

The main contributions of the present work to the second strain gradient modelling of the elastic behaviour of nano-objects are the following:

- A clear distinction was made between the features of the model responsible for free surface relaxation effects and pure surface elasticity arising during the straining of nano-objects. The surface energy property of the medium is directly related to the initial higher order stress, or cohesion modulus, b_0, while the apparent surface stress effects are induced by the coupling moduli, c_i, in the elastic potential (23). They are uncorrelated in the sense that surface elasticity effects can arise for vanishing b_0, and vice versa.
- A thorough analysis of a one-dimensional case was presented for the deformation close to a traction free surface in a half-space and in a free-standing film. Decaying, aperiodic and oscillating modes were distinguished in terms of the values of the higher order elastic moduli taking stability requirements into account, something which was not done in earlier contributions on the topic.
- The role of the coupling moduli in the modification of apparent elastic properties was highlighted for the first time, by means of analytical and numerical solutions in tension and shear of thin strips. This role is apparent in the following simple one-dimensional elasticity relation which came out in this work:

$$\sigma_{11} = (\lambda + 2\mu)\varepsilon_{11} + \bar{c}\ \varepsilon_{11,11} \tag{84}$$

This relation connects the simple stress components, σ_{11}, to the second derivative of the strain.

- The derived analytical expression (75) of the apparent shear modulus of a material strip under shear clearly shows that the second strain gradient theory is necessary to model size-dependent apparent shear properties in isotropic media. In particular, the first strain gradient theory is not sufficient for that purpose, which settles the existing debate of the required order of the theory for the gradient continuum modelling of nano-elastic effects. This statement is however limited to the isotropic case.
- Finite Element simulations of second strain gradient elasticity, based on the second order micromorphic continuum with internal constraints, were performed for the first time. The inhomogeneous strain distribution close to free surfaces in a strip in tension was simulated as a function of plate thickness. The model was also used for the simulation of surface relaxation induced by the cohesion hyperstress b_0 in an elastic matrix containing a periodic distribution of nano-pores.
- Some of the material parameters of the model were estimated from the size-dependent apparent moduli of ZnO nano-wires in tension. This represents a first step towards systematic identification of higher order elastic moduli from experimental testing on nano-objects, or, possibly from complementary atomistic simulations.

This work represents a contribution to the use of higher grade continuum theories for the modelling of nano-elasticity. The approach has the advantage that it does not geometrically distinguish a boundary region from the bulk. Instead, boundary layers naturally arise from the extra-boundary conditions associated with higher grade continuum theories.

The main limitation of the work is the restriction to the isotropic case highlighting the main features of second strain gradient elasticity. Most crystalline nano-objects display an anisotropic material response. Mindlin's second strain gradient theory must now be extended to the anisotropic case which involves a large number of higher order elastic moduli. The symmetry classes and corresponding independent elastic moduli were recently determined for 6-th order tensors arising in first strain gradient elasticity, see Auffray et al. (2013b), Olive and Auffray (2014), and Auffray (2014). The mathematical tools presented in the latter references can be used to extend these representations to the 8th order tensor of elastic moduli arising in the second strain gradient model, together with odd-order coupling tensors.

The systematic identification of such a huge number of material parameters represents a major task in future developments of the approach. They can be determined for instance from the effective size-dependent apparent elastic properties of nano-porous materials, but also from molecular dynamics or ab initio results (Villain et al., 2004; Maranganti and Sharma, 2007; Yvonnet et al., 2012).

Non-positive definite higher order moduli were found to be necessary to obtain stiffer properties both in shear and plane strain tension. This contributes to the debate on the identification of non-positive higher order or surface elasticity properties sometimes found from atomistic simulations, as discussed by Maranganti and Sharma (2007), Yvonnet et al. (2008), and Javili et al. (2012). The relevance of the proposed parameters and the possible need for higher order regularisation remain open questions which require a thorough analysis of the well-posedness of the associated variational problem.

Global stability of nano-object undergoing oscillating straining modes should be investigated.

The links between surface elasticity theory in the spirit of the Gurtin–Murdoch model and second strain gradient elasticity remain to be established more precisely. For that purpose, it is anticipated that an asymptotic analysis of the second strain gradient model close to a free or loaded surface can be performed to identify the surface properties of an equivalent generalised surface model from the bulk higher order elasticity moduli. Such an asymptotic analysis may even provide new surface properties not yet accounted for in the existing surface models. Further developments also include the consideration of elasticity with defects and interfaces (Upadhyay et al., 2012; Dingreville et al., 2014).

Acknowledgments

This work is part of the NANOCRYSTAL Project ANR-07-BLAN-0186. Financial support of ANR is gratefully acknowledged.

Appendix A. Formulation of the second order micromorphic model

This section gives the main equations of the micromorphic approach used for a numerical implementation of the second gradient of strain theory presented in Section 2. The second order micromorphic approach is formulated following Germain's general micromorphic theory introduced for the first time in Germain (1973b). First, its balance and constitutive equations are given. Then, internal constraints are enforced to control the micro-deformations and obtain the second strain gradient theory as a special case of the second order micromorphic model.

A.1. Balance equations

Two micro-deformation variables, $\underline{\chi}$ and $\underline{\underline{\chi}}$, are introduced for each material point as second-rank and third-rank tensors respectively in which the following symmetry properties are considered:

$$\chi_{ij} = \chi_{ji}, \quad \chi_{ijk} = \chi_{jik}. \tag{85}$$

$\underline{\chi}$ is called the microstrain tensor. The degrees of freedom of each material point are

$$DOF := \left\{ \underline{\boldsymbol{u}}, \underline{\chi}, \underline{\underline{\chi}} \right\}, \left\{ u_i, \chi_{ij}, \chi_{ijk} \right\}, \tag{86}$$

where the components of $\underline{\chi}$ and $\underline{\underline{\chi}}$ are introduced as independent degrees of freedom in addition to the usual displacement vector. In 2D (plane strain), with the symmetry properties (85), nine degrees of freedom are introduced in addition to the 2 displacement components, u_i. This number reaches twenty-four in 3D. Following Germain, the generalised power of internal forces is a linear form with respect to the degrees of freedom and their first gradient:

$$\begin{aligned} p^{(i)} &= \underset{\sim}{\sigma} : \dot{\underline{\varepsilon}} + \underset{\sim}{\boldsymbol{s}} : \left(\dot{\underline{\varepsilon}} - \dot{\underline{\chi}} \right) + \underline{\boldsymbol{S}} \vdots \left(\dot{\underline{\chi}} \otimes \nabla \right) + \underline{\boldsymbol{s}} \vdots \left(\dot{\underline{\chi}} \otimes \nabla - \dot{\underline{\underline{\chi}}} \right) + \underline{\underline{\boldsymbol{S}}} :: \left(\dot{\underline{\underline{\chi}}} \otimes \nabla \right), \\ p^{(i)} &= \sigma_{ij}\, \dot{\varepsilon}_{ij} + s_{ij} \left(\dot{\varepsilon}_{ij} - \dot{\chi}_{ij} \right) + S_{ijk}\, \dot{\chi}_{ij,k} + s_{ijk} \left(\dot{\chi}_{ij,k} - \dot{\chi}_{ijk} \right) + S_{ijkl}\, \dot{\chi}_{ijk,l} \end{aligned} \tag{87}$$

Here, $\underset{\sim}{\sigma}$, $\underline{\boldsymbol{S}}$ and $\underline{\underline{\boldsymbol{S}}}$ are the simple, double and triple stress tensors, respectively. Relative stress tensors $\underset{\sim}{\boldsymbol{s}}$ and $\underline{\boldsymbol{s}}$ are introduced as reactions to the difference of strain and microstrain, and of third order microdeformation and the gradient of microstrain. The power of internal forces in a domain V, with smooth boundary ∂V, is then

$$\begin{aligned} \mathcal{P}^{(i)} &= \int_V p^{(i)}\, dV \\ &= \int_V \left[\underset{\sim}{\sigma} : \dot{\underline{\varepsilon}} + \underset{\sim}{\boldsymbol{s}} : \left(\dot{\underline{\varepsilon}} - \dot{\underline{\chi}} \right) + \underline{\boldsymbol{S}} \vdots \left(\dot{\underline{\chi}} \otimes \nabla \right) + \underline{\boldsymbol{s}} \vdots \left(\dot{\underline{\chi}} \otimes \nabla - \dot{\underline{\underline{\chi}}} \right) + \underline{\underline{\boldsymbol{S}}} :: \left(\dot{\underline{\underline{\chi}}} \otimes \nabla \right) \right] dV \\ &= - \int_V \left\{ \left[\left(\underset{\sim}{\sigma} + \underset{\sim}{\boldsymbol{s}} \right) . \nabla \right] . \dot{\underline{\boldsymbol{u}}} + \left[\underset{\sim}{\boldsymbol{s}} + \left(\underline{\boldsymbol{S}} + \underline{\boldsymbol{s}} \right) . \nabla \right] : \dot{\underline{\chi}} + \left(\underline{\boldsymbol{s}} + \underline{\underline{\boldsymbol{S}}} . \nabla \right) \vdots \dot{\underline{\underline{\chi}}} \right\} dV \\ &\quad + \int_{\partial V} \underline{\boldsymbol{n}} . \left[\left(\underset{\sim}{\sigma} + \underset{\sim}{\boldsymbol{s}} \right) . \dot{\underline{\boldsymbol{u}}} + \left(\underline{\boldsymbol{S}} + \underline{\boldsymbol{s}} \right) : \dot{\underline{\chi}} + \underline{\underline{\boldsymbol{S}}} \vdots \dot{\underline{\underline{\chi}}} \right] dS \\ &= \int_{\partial V} \left(\underline{\boldsymbol{t}} . \dot{\underline{\boldsymbol{u}}} + \underline{\boldsymbol{t}} : \dot{\underline{\chi}} + \underline{\underline{\boldsymbol{t}}} \vdots \dot{\underline{\underline{\chi}}} \right) dS, \end{aligned} \tag{88a}$$

$$\begin{aligned}\mathcal{P}^{(i)} &= \int_V \left[\sigma_{ij}\,\dot{e}_{ij} + s_{ij}\left(\dot{e}_{ij} - \dot{\chi}_{ij}\right) + S_{ijk}\,\dot{\chi}_{ij,k} + s_{ijk}\left(\dot{\chi}_{ij,k} - \dot{\chi}_{ijk}\right) + S_{ijkl}\,\dot{\chi}_{ijk,l}\right] dV \\ &= -\int_V \left[\left(\sigma_{ij} + s_{ij}\right)_{,j}\dot{u}_i + \left(s_{ij} + \left(S_{ijk} + s_{ijk}\right)_{,k}\right)\dot{\chi}_{ij} + \left(s_{ijk} + S_{ijkl,l}\right)\dot{\chi}_{ijk}\right] dV \\ &\quad + \int_{\partial V}\left[\left(\sigma_{ij} + s_{ij}\right)n_j\,\dot{u}_i + \left(S_{ijk} + s_{ijk}\right)n_k\,\dot{\chi}_{ij} + S_{ijkl}\,n_l\,\dot{\chi}_{ijk}\right] dS \\ &= \int_{\partial V}\left(t_i\dot{u}_i + t_{ij}\dot{\chi}_{ij} + t_{ijk}\dot{\chi}_{ijk}\right) dS.\end{aligned} \tag{88b}$$

The method of virtual power is applied to obtain the balance field equations, in the absence of volume forces for the sake of brevity,

$$\left(\underset{\sim}{\sigma} + \underset{\sim}{s}\right).\,\nabla = 0, \quad \left(\sigma_{ij} + s_{ij}\right)_{,j} = 0, \tag{89a}$$

$$\underset{\sim}{s} + \left(\underline{\underline{S}} + \underline{\underline{s}}\right).\,\nabla = 0, \quad s_{ij} + \left(S_{ijk} + s_{ijk}\right)_{,k} = 0, \tag{89b}$$

$$\underline{\underline{s}} + \underline{\underline{\underline{S}}}.\,\nabla = 0, \quad s_{ijk} + S_{ijkl,l} = 0, \tag{89c}$$

The corresponding boundary conditions are also obtained from Eq. (88b) as

$$\underline{t} = \left(\underset{\sim}{\sigma} + \underset{\sim}{s}\right).\,\underline{n}, \quad t_i = \left(\sigma_{ij} + s_{ij}\right)n_j, \tag{90a}$$

$$\underset{\sim}{t} = \left(\underline{\underline{S}} + \underline{\underline{s}}\right).\,\underline{n}, \quad t_{ij} = \left(S_{ijk} + s_{ijk}\right)n_k, \tag{90b}$$

$$\underline{\underline{t}} = \underline{\underline{\underline{S}}}\,.\,\underline{n}, \quad t_{ijk} = S_{ijkl}\,n_l. \tag{90c}$$

Note that in this micromorphic approach, the generalised surface tractions $\underline{t}$, $\underset{\sim}{t}$ and $\underline{\underline{t}}$ are first, second and third order tensors, respectively. In contrast, in the second strain gradient theory presented of Section 2.1, the tractions are vectors. The difference comes from the fact that in the second strain gradient theory, there are no additional DOFs independent of displacement. The previous expressions are consistent with the ranks of the chosen micro-deformations.

A.2. Constitutive equations

The free energy function is assumed to have the five following arguments:

$$\Psi\left(\underset{\sim}{\varepsilon},\ \underset{\sim}{e} := \underset{\sim}{\varepsilon} - \underset{\sim}{\chi},\ \underline{\underline{K}} := \underline{\chi} \otimes \nabla,\ \underline{\underline{e}} := \underline{\underline{K}} - \underline{\chi},\ \underline{\underline{\underline{K}}} := \underline{\underline{\chi}} \otimes \nabla\right) \tag{91}$$

where $\underline{\underline{K}}$ and $\underline{\underline{\underline{K}}}$ are notations for the first gradients of microstrain and second order microdeformation. The relative strain tensors $\underline{\underline{e}}$ and $\underline{\underline{\underline{e}}}$ measure the differences between the strain $\underset{\sim}{\varepsilon}$ and the gradient $\underline{\underline{K}}$ with their associated micro-deformations. In 2D, $\underline{\underline{K}}$, $\underline{\underline{\underline{K}}}$, $\underset{\sim}{e}$ and $\underline{\underline{e}}$ respectively have six, twelve, three and six independent components. With these notations, the power density of internal forces (87) becomes

$$\begin{aligned}p^{(i)} &= \underset{\sim}{\sigma} : \dot{\underset{\sim}{\varepsilon}} + \underset{\sim}{s} : \dot{\underset{\sim}{e}} + \underline{\underline{S}} \vdots \dot{\underline{\underline{K}}} + \underline{\underline{s}} \vdots \dot{\underline{\underline{e}}} + \underline{\underline{\underline{S}}} :: \dot{\underline{\underline{\underline{K}}}}, \\ p^{(i)} &= \sigma_{ij}\dot{\varepsilon}_{ij} + s_{ij}\dot{e}_{ij} + S_{ijk}\dot{K}_{ijk} + s_{ijk}\dot{e}_{ijk} + S_{ijkl}\dot{K}_{ijkl}.\end{aligned} \tag{92}$$

The state laws are obtained using the free energy function (91):

$$\underset{\sim}{\sigma} = \rho\frac{\partial\Psi}{\partial\underset{\sim}{\varepsilon}}, \quad \underline{\underline{S}} = \rho\frac{\partial\Psi}{\partial\underline{\underline{K}}}, \quad \underline{\underline{\underline{S}}} = \rho\frac{\partial\Psi}{\partial\underline{\underline{\underline{K}}}}, \tag{93}$$

$$\underset{\sim}{s} = \rho\frac{\partial\Psi}{\partial\underset{\sim}{e}}, \quad \underline{\underline{s}} = \rho\frac{\partial\Psi}{\partial\underline{\underline{e}}}. \tag{94}$$

The simple, double and triple stress tensors, $\underset{\sim}{\sigma}$, $\underline{\underline{S}}$ and $\underline{\underline{\underline{S}}}$, and the relative stress tensors, $\underset{\sim}{s}$ and $\underline{\underline{s}}$, have the same symmetry properties as their associated strain tensors, $\underset{\sim}{\varepsilon}$, $\underline{\underline{K}}$, $\underline{\underline{\underline{K}}}$, $\underset{\sim}{e}$ and $\underline{\underline{e}}$ respectively. Note that the symmetry properties considered here (85) are different from the symmetry properties (8) of the second strain gradient theory. Consequently, the independent components of the strain and stress tensors of the micromorphic approach are different from those of the second strain gradient theory. Next, we consider linearised elasticity constitutive equations in the general form for the simple, double and triple stress tensors,

$$\underset{\sim}{\sigma} = \underset{\approx}{\Lambda} : \underset{\sim}{\varepsilon} + \overbrace{\underset{\approx}{\underset{\sim}{C}} :: \underset{\approx}{\underset{\sim}{K}}}^{\text{coupling}}, \quad \underset{\sim}{\underline{S}} = \underset{\approx}{\underline{A}} \vdots \underset{\sim}{\underline{K}}, \quad \underset{\approx}{\underline{S}} = \underset{\approx}{\underline{B}} :: \underset{\approx}{\underline{K}} + \overbrace{\underset{\approx}{\underset{\sim}{C}}^{T} : \underset{\sim}{\varepsilon}}^{\text{coupling}} + \overbrace{b_0 \underset{\approx}{\mathbf{1}}}^{\text{initial stress}}, \tag{95}$$

and for the relative stress tensors,

$$\underset{\sim}{s} = \underset{\approx}{\underset{\chi}{H}}^{a} : \underset{\sim}{e}, \quad \underset{\sim}{\underline{s}} = \underset{\approx}{\underset{\chi}{H}}^{b} \vdots \underset{\sim}{\underline{e}}. \tag{96}$$

A simplified form of these constitutive elasticity tensors is adopted in the present work:

$$\underset{\approx}{\underline{A}} = A \underset{\approx}{\mathbf{1}}, \quad \underset{\approx}{\underline{B}} = B \underset{\approx}{\mathbf{1}}, \quad \underset{\approx}{\underset{\chi}{H}}^{a} = H_{\chi}^{a} \underset{\approx}{\mathbf{1}}, \quad \underset{\approx}{\underset{\chi}{H}}^{b} = H_{\chi}^{b} \underset{\approx}{\mathbf{1}}, \tag{97}$$

where A, B, H_{χ}^{a} and H_{χ}^{b} are the generalised elastic moduli and unity tensors of order 4, 6 and 8 operating on tensors with suited order and symmetry properties were introduced. Only one higher order modulus is introduced for each higher order constitutive tensor. This is in contrast to the a_i and $b_{i,\, i\neq 0}$ introduced in the isotropic second strain gradient theory. This considerably simplifies the formulation of the present model and should be regarded as a first step for the exploration of such higher order theories. Reduced numbers of higher elastic moduli were also used in strain gradient elasticity by Ru and Aifantis (1993), Shu (1998), and Forest and Aifantis (2010) and second strain gradient elasticity (Lazar et al., 2006a,b; Polizzotto, 2013). Note that, in this simplified form, no coupling is considered with respect to the relative strains. A more general isotropic formulation should be considered in the future. The coupling terms appearing in $\underset{\sim}{\sigma}$ and $\underset{\approx}{\underline{S}}$ have the same origin as the coupling terms of the constitutive equations (24a) and (24c) from Mindlin's theory. They introduce additional terms proportional to some components, K_{ijkl}, in the simple stress tensor and additional terms proportional to the strain components, ε_{ij}, in the triple stress tensor. As this coupling plays a key role in surface elasticity effects, no simplification is made here. The initial stress appearing in some components S_{ijkl} is linked to the initial higher order stress, or cohesive modulus, b_0, and consequently to surface energy. In order to define the additional terms, coming from the coupling and the initial stress, that have to be introduced in $\underset{\sim}{\sigma}$ and $\underset{\approx}{\underline{S}}$, the corresponding part $\rho\Psi^{\text{cpl}}(\underset{\sim}{\varepsilon}, \underset{\approx}{\underline{K}})$ of the free energy density function is written, in the isotropic case, as

$$\begin{aligned}\rho\Psi^{\text{cpl}} = {} & C_1\, \varepsilon_{ii}\, K_{kkll} + C_2\, \varepsilon_{ii}\, K_{klkl} + C_3\, \varepsilon_{ii}\, K_{kllk} + C_4\, \varepsilon_{ij}\, K_{ijkk} + C_5\, \varepsilon_{ij}\, K_{ikjk} \\ & + C_6\, \varepsilon_{ij}\, K_{ikkj} + C_7\, \varepsilon_{ij}\, K_{jikk} + C_8\, \varepsilon_{ij}\, K_{jkik} + C_9\, \varepsilon_{ij}\, K_{jkki} + C_{10}\, \varepsilon_{ij}\, K_{kkij} \\ & + C_{11}\, \varepsilon_{ij}\, K_{kikj} + C_{12}\, \varepsilon_{ij}\, K_{kijk} + C_{13}\, \varepsilon_{ij}\, K_{kkji} + C_{14}\, \varepsilon_{ij}\, K_{kjki} + C_{15}\, \varepsilon_{ij}\, K_{kjik} \\ & + \frac{1}{3} b_0 \Big(K_{kkll} + K_{klkl} + K_{kllk} \Big),\end{aligned} \tag{98}$$

where the symmetry property $K_{ijkl} = K_{jikl}$ is not taken into account as needed to compute the stress tensors by mean of partial derivatives. The state laws (93) are used to derive the stress and relative stress tensors and the symmetry properties (85) are applied to the results. The following constitutive equations are finally obtained for the stress tensors:

$$\begin{aligned}\sigma_{pq} = {} & \lambda\, \varepsilon_{ii}\, \delta_{pq} + 2\mu\, \varepsilon_{pq} + c_1'\, K_{iijj}\, \delta_{pq} + \frac{1}{2} c_2' \Big(K_{iipq} + K_{iiqp} \Big) + c_3'\, K_{pqii} \\ & + c_4'\, K_{ijij}\, \delta_{pq} + \frac{1}{2} c_5' \Big(K_{piqi} + K_{iqpi} \Big) + \frac{1}{2} c_6' \Big(K_{piiq} + K_{iqip} \Big),\end{aligned} \tag{99a}$$

$$S_{pqr} = A\, K_{pqr}, \tag{99b}$$

$$\begin{aligned}S_{pqrs} = {} & B\, K_{pqrs} + c_1'\, \varepsilon_{ii}\, \delta_{pq}\delta_{rs} + c_2'\, \varepsilon_{rs}\, \delta_{pq} + c_3'\, \varepsilon_{pq}\, \delta_{rs} + \frac{1}{2} c_4'\, \varepsilon_{ii} \Big(\delta_{pr}\delta_{qs} + \delta_{qr}\delta_{ps} \Big) \\ & + \frac{1}{2} c_5' \Big(\varepsilon_{ir} \big(\delta_{ip}\delta_{qs} + \delta_{iq}\delta_{ps} \big) + \varepsilon_{is} \big(\delta_{ip}\delta_{qr} + \delta_{iq}\delta_{pr} \big) \Big) + \frac{1}{3} b_0 \delta_{pqrs},\end{aligned} \tag{99c}$$

with $\delta_{ijkl} = \delta_{ij}\delta_{kl} + \delta_{ik}\delta_{jl} + \delta_{jk}\delta_{il}$, and for the relative stress tensors:

$$s_{pq} = H_{\chi}^{a}\, e_{pq}, \quad s_{pqr} = H_{\chi}^{b}\, e_{pqr}. \tag{100}$$

The coefficients c_i' are the coupling moduli in the same way as the c_i of Mindlin's theory. They are related to the coefficients C_i of the non-symmetrised free energy density (98) as

$$\begin{aligned}& c_1' = C_1, \quad c_2' = C_{10} + C_{13}, \quad c_3' = C_4 + C_7, \quad c_4' = C_2 + C_3, \\ & c_5' = C_5 + C_8 + C_{12} + C_{15}, \quad c_6' = C_6 + C_9 + C_{11} + C_{14}.\end{aligned} \tag{101}$$

Note that the symmetry properties (85) reduce the number of coupling coefficients from fifteen to six. The dimensions of the moduli and of the strain and stress tensors' components of the present model are given in Table 3.

A.3. Internal constraints

The moduli H_{χ}^{a} and H_{χ}^{b} in Eqs. (96) are used to enforce constraints on the differences between $\underset{\sim}{\varepsilon}$ and $\underset{\sim}{\chi}$ and between the gradient of $\underset{\sim}{\chi}$ and $\underset{\approx}{\chi}$ respectively. These moduli act as penalty factors to force the relative strains to be negligibly small. For that purpose, H_{χ}^{a} and H_{χ}^{b} have to be sufficiently high. This internal constraint then reads

$$\begin{aligned} &\underset{\sim}{\chi} \equiv \underset{\sim}{\varepsilon}, \quad \underset{\approx}{\chi} \equiv \underline{\underline{\boldsymbol{K}}} \equiv \underset{\sim}{\chi} \otimes \nabla \equiv \underset{\sim}{\varepsilon} \otimes \nabla, \\ &\chi_{ij} \equiv \varepsilon_{ij}, \quad \chi_{ijk} \equiv K_{ijk} \equiv \chi_{ij,k} \equiv \varepsilon_{ij,k}. \end{aligned} \tag{102}$$

In the limit of infinitely high values of the moduli H_{χ}^{a} and H_{χ}^{b}, the proposed second order micromorphic theory therefore coincides with Mindlin's second strain gradient theory.

The constraints (102) are now used to identify the coupling moduli c_i' that become equivalent to the c_i of Eq. (23). The expression of $\underset{\sim}{\sigma}$ can then be written as a function of the components of the strain tensor and of its second gradient:

$$\begin{aligned} \sigma_{pq} = {} & \lambda\, \varepsilon_{ii}\, \delta_{pq} + 2\mu\, \varepsilon_{pq} + c_1'\, \varepsilon_{ii,jj}\, \delta_{pq} + c_2'\, \varepsilon_{ii,pq} + c_3'\, \varepsilon_{pq,ii} \\ & + c_4'\, \varepsilon_{ij,ij}\, \delta_{pq} + \frac{1}{2}\, c_5'\Big(\varepsilon_{pi,qi} + \varepsilon_{iq,pi}\Big) + \frac{1}{2}\, c_6'\Big(\varepsilon_{pi,iq} + \varepsilon_{iq,ip}\Big). \end{aligned} \tag{103}$$

With the compatibility equation given in 2D as

$$\varepsilon_{kk,ll} + \varepsilon_{ll,kk} = 2\, \varepsilon_{kl,kl}, \tag{104}$$

the expression (103) becomes

$$\begin{aligned} \sigma_{pq} = {} & \lambda\, \varepsilon_{ii}\, \delta_{pq} + 2\mu\, \varepsilon_{pq} + \left(c_1' + c_4'\right)\varepsilon_{ii,jj}\, \delta_{pq} + \left(c_2' + \frac{c_5' + c_6'}{2}\right)\varepsilon_{ii,pq} \\ & + \left(c_3' + \frac{c_5' + c_6'}{2}\right)\varepsilon_{pq,ii}. \end{aligned} \tag{105}$$

Similarly, the expression of $\underset{\sim}{\sigma}$ derived in Mindlin's theory is also written as a function of ε_{ij} and $\varepsilon_{ij,kl}$. For that purpose, the gradients of the displacement have to be expressed in terms of gradients of the strain. Toupin's relation linking gradient of strain and second gradient of displacement,

$$u_{i,jk} = \varepsilon_{ij,k} + \varepsilon_{ki,j} - \varepsilon_{jk,i}, \tag{106}$$

is used and recalling that Eq. (6) gives $\varepsilon_{ijkl} = u_{i,jkl}$, Eq. (24a) becomes

$$\sigma_{pq} = \lambda\, \varepsilon_{ii}\, \delta_{pq} + 2\,\mu\, \varepsilon_{pq} + c_1\, \varepsilon_{ii,jj}\, \delta_{pq} + c_2\, \varepsilon_{ii,pq} + c_3\, \varepsilon_{pq,ii}. \tag{107}$$

The identification of relations (105) and (107) then leads to

$$c_1' + c_4' \equiv c_1, \quad c_2' + \frac{c_5' + c_6'}{2} \equiv c_2, \quad c_3' + \frac{c_5' + c_6'}{2} \equiv c_3. \tag{108}$$

Appendix B. Main features of the finite element implementation

The purpose of this appendix is to give the main features of the finite element implementation of the second order micromorphic model presented in Appendix A. For the sake of simplicity, the finite element implementation presented here is limited to 2D under plane strain conditions. The notations and general algorithm for the finite element formulation are taken from Besson et al. (2009).

The chosen elements are isoparametric, i.e., the same shape functions are used to interpolate nodal coordinates and mechanical degrees of freedom. They are quadratic with reduced integration and have two displacement and nine micro-deformation degrees of freedom,

Table 3
Dimensions of the coefficients, strains and stresses used in the second order micromorphic model.

Coefficient	Dimension	Strain	Dimension	Stresses	Dimension
λ, μ	MPa ≡ N mm^{-2}	ε_{ij}, χ_{ij}, e_{ij}	dimensionless	σ_{ij}	MPa ≡ N mm^{-2}
A, c_i', b_0	MPa mm^2 ≡ N	χ_{ijk}, K_{ijk}, e_{ijk}	mm^{-1}	S_{ijk}	MPa mm ≡ N mm^{-1}
B	MPa mm^4 ≡ N mm^2	K_{ijkl}	mm^{-2}	S_{ijkl}	MPa mm^2 ≡ N

$$[DOF]^T = \left[u_1 \;\; u_2 \;\; \chi_{11} \;\; \chi_{22} \;\; \chi_{12} \;\; \chi_{111} \;\; \chi_{221} \;\; \chi_{122} \;\; \chi_{222} \;\; \chi_{112} \;\; \chi_{121}\right]. \tag{109}$$

The B-matrix is the transformation matrix used to calculate the components of the strain tensors (ε_{ij}, K_{ijk} and K_{ijkl}) and relative strain tensors (e_{ij} and e_{ijk}) from the degrees of freedom as

$$[STRAIN] = [\mathrm{B}_{matrix}][DOF]. \tag{110}$$

This matrix is given in Fig. 16. In the sequel of the appendix, blank parts of matrices used in the finite element formulation are filled with 0. The shape function N is such that, for example, $\varepsilon_{11} = N_{,1}\, u_1 = u_{1,1}$ and $e_{11} = N_{,1}\, u_1 - N\, \chi_{11} = u_{1,1} - \chi_{11}$. The algebra of 2D symmetric second order tensors is used, which introduces the factor $\sqrt{2}$ in shear components. The components of the stress tensors (σ_{ij}, S_{ijk} and S_{ijkl}) and relative stress tensors (s_{ij} and s_{ijk}) are computed as

$$[STRESS] = [D][STRAIN] + [b_0], \tag{111a}$$

$$\begin{bmatrix} [\underset{\sim}{\boldsymbol{\sigma}}] \\ [\underset{\sim}{\boldsymbol{s}}] \\ [\underset{\cong}{\boldsymbol{S}}] \\ [\underset{\sim}{\boldsymbol{s}}] \\ [\underset{\approx}{\boldsymbol{S}}] \end{bmatrix} = \begin{bmatrix} [\Lambda] & & & & [C] \\ & [H_\chi^a] & & & \\ & & [A] & & \\ & & & [H_\chi^b] & \\ [C]^T & & & & [B] \end{bmatrix} \begin{bmatrix} [\underset{\sim}{\boldsymbol{\varepsilon}}] \\ [\underset{\sim}{\boldsymbol{e}}] \\ [\underset{\cong}{\boldsymbol{K}}] \\ [\underset{\sim}{\boldsymbol{e}}] \\ [\underset{\approx}{\boldsymbol{K}}] \end{bmatrix} + \begin{bmatrix} \\ \\ \\ \\ b_0 [\underset{\approx}{\mathbf{1}}] \end{bmatrix}. \tag{111b}$$

where the components of the simple, double and triple stress tensors and the relative stress tensors are ranked in matrix form as follows:

$$\begin{bmatrix} \varepsilon_{11} \\ \varepsilon_{22} \\ \varepsilon_{33} \\ \sqrt{2}\varepsilon_{12} \\ \\ e_{11} \\ e_{22} \\ \sqrt{2}e_{12} \\ \\ K_{111} \\ K_{221} \\ \sqrt{2}K_{122} \\ K_{222} \\ K_{112} \\ \sqrt{2}K_{121} \\ \\ e_{111} \\ e_{221} \\ \sqrt{2}e_{122} \\ e_{222} \\ e_{112} \\ \sqrt{2}e_{121} \\ \\ K_{1111} \\ K_{2211} \\ \sqrt{2}K_{1221} \\ K_{2222} \\ K_{1122} \\ \sqrt{2}K_{1212} \\ K_{1112} \\ K_{2212} \\ \sqrt{2}K_{1222} \\ K_{2221} \\ K_{1121} \\ \sqrt{2}K_{1211} \end{bmatrix} = \begin{bmatrix} N_{,1} & 0 & & & & & & & & & & \\ 0 & N_{,2} & & & & & & & & & & \\ 0 & 0 & & & & & & & & & & \\ N_{,2}/\sqrt{2} & N_{,1}/\sqrt{2} & & & & & & & & & & \\ \\ N_{,1} & 0 & -N & 0 & 0 & & & & & & & \\ 0 & N_{,2} & 0 & -N & 0 & & & & & & & \\ N_{,2}/\sqrt{2} & N_{,1}/\sqrt{2} & 0 & 0 & -\sqrt{2}N & & & & & & & \\ \\ & & N_{,1} & 0 & 0 & & & & & & & \\ & & 0 & N_{,1} & 0 & & & & & & & \\ & & 0 & 0 & \sqrt{2}N_{,2} & & & & & & & \\ & & 0 & N_{,2} & 0 & & & & & & & \\ & & N_{,2} & 0 & 0 & & & & & & & \\ & & 0 & 0 & \sqrt{2}N_{,1} & & & & & & & \\ \\ & & N_{,1} & 0 & 0 & -N & 0 & 0 & 0 & 0 & 0 & \\ & & 0 & N_{,1} & 0 & 0 & -N & 0 & 0 & 0 & 0 & \\ & & 0 & 0 & \sqrt{2}N_{,2} & 0 & 0 & -\sqrt{2}N & 0 & 0 & 0 & \\ & & 0 & N_{,2} & 0 & 0 & 0 & 0 & -N & 0 & 0 & \\ & & N_{,2} & 0 & 0 & 0 & 0 & 0 & 0 & -N & 0 & \\ & & 0 & 0 & \sqrt{2}N_{,1} & 0 & 0 & 0 & 0 & 0 & -\sqrt{2}N & \\ \\ & & & & & N_{,1} & 0 & 0 & 0 & 0 & 0 & \\ & & & & & 0 & N_{,1} & 0 & 0 & 0 & 0 & \\ & & & & & 0 & 0 & \sqrt{2}N_{,1} & 0 & 0 & 0 & \\ & & & & & 0 & 0 & 0 & N_{,2} & 0 & 0 & \\ & & & & & 0 & 0 & 0 & 0 & N_{,2} & 0 & \\ & & & & & 0 & 0 & 0 & 0 & 0 & \sqrt{2}N_{,2} & \\ & & & & & N_{,2} & 0 & 0 & 0 & 0 & 0 & \\ & & & & & 0 & N_{,2} & 0 & 0 & 0 & 0 & \\ & & & & & 0 & 0 & \sqrt{2}N_{,2} & 0 & 0 & 0 & \\ & & & & & 0 & 0 & 0 & N_{,1} & 0 & 0 & \\ & & & & & 0 & 0 & 0 & 0 & N_{,1} & 0 & \\ & & & & & 0 & 0 & 0 & 0 & 0 & \sqrt{2}N_{,1} & \end{bmatrix} \begin{bmatrix} u_1 \\ u_2 \\ \chi_{11} \\ \chi_{22} \\ \chi_{12} \\ \chi_{111} \\ \chi_{221} \\ \chi_{122} \\ \chi_{222} \\ \chi_{112} \\ \chi_{121} \end{bmatrix}$$

Fig. 16. B-matrix used in the finite element code to calculate the components of the strain and relative strain tensors from the nodal degrees of freedom. Blank parts of the matrix are filled with 0.

$$
\begin{aligned}
&[\underset{\sim}{\boldsymbol{\sigma}}]^T = \begin{bmatrix} \sigma_{11} & \sigma_{22} & \sigma_{33} & \sqrt{2}\,\sigma_{12} \end{bmatrix},\\
&[\underset{\sim}{\boldsymbol{S}}]^T = \begin{bmatrix} S_{111} & S_{221} & \sqrt{2}\,S_{122} & S_{222} & S_{112} & \sqrt{2}\,S_{121} \end{bmatrix},\\
&[\underset{\approx}{\boldsymbol{S}}]^T = \begin{bmatrix} S_{1111} & S_{2211} & \sqrt{2}\,S_{1221} & S_{2222} & S_{1122} & \sqrt{2}\,S_{1212} & S_{1112} & S_{2212} & \sqrt{2}\,S_{1222} & S_{2221} & S_{1121} & \sqrt{2}\,S_{1211} \end{bmatrix},\\
&[\underset{\sim}{\boldsymbol{s}}]^T = \begin{bmatrix} s_{11} & s_{22} & s_{12} \end{bmatrix}, \quad [\underset{\sim}{\boldsymbol{s}}]^T = \begin{bmatrix} s_{111} & s_{221} & s_{122} & s_{222} & s_{112} & s_{121} \end{bmatrix}.
\end{aligned}
\tag{112}
$$

The strain and relative strain tensors are computed in the same way:

$$
\begin{aligned}
&[\underset{\sim}{\boldsymbol{\varepsilon}}]^T = \begin{bmatrix} \varepsilon_{11} & \varepsilon_{22} & \varepsilon_{33} & \sqrt{2}\,\varepsilon_{12} \end{bmatrix}, \quad [\underset{\sim}{\boldsymbol{K}}]^T = \begin{bmatrix} K_{111} & K_{221} & \sqrt{2}\,K_{122} & K_{222} & K_{112} & \sqrt{2}\,K_{121} \end{bmatrix},\\
&[\underset{\approx}{\boldsymbol{K}}]^T = \begin{bmatrix} K_{1111} & K_{2211} & \sqrt{2}\,K_{1221} & K_{2222} & K_{1122} & \sqrt{2}\,K_{1212} & K_{1112} & K_{2212} & \sqrt{2}\,K_{1222} & K_{2221} & K_{1121} & \sqrt{2}\,K_{1211} \end{bmatrix},\\
&[\underset{\sim}{\boldsymbol{e}}]^T = \begin{bmatrix} e_{11} & e_{22} & e_{12} \end{bmatrix}, \quad [\underset{\sim}{\boldsymbol{e}}]^T = \begin{bmatrix} e_{111} & e_{221} & e_{122} & e_{222} & e_{112} & e_{121} \end{bmatrix}.
\end{aligned}
\tag{113}
$$

The invertible matrix $[D]$ is the matrix of the elastic moduli in which four distinct parts can be noted. $[A]$ contains the classical elastic moduli. $[A]$ and $[B]$ are the diagonal matrices of the generalised moduli A and B that are related to the first and second strain gradients respectively and defined as

$$
\begin{bmatrix} A \end{bmatrix} = \begin{bmatrix} A & & \\ & \ddots & \\ & & A \end{bmatrix}, \quad \begin{bmatrix} B \end{bmatrix} = \begin{bmatrix} B & & \\ & \ddots & \\ & & B \end{bmatrix}.
\tag{114}
$$

$[A]$ and $[B]$ are the matrix forms of a sixth rank tensor and a eighth rank tensor respectively. The blocks $[C]$ and $[C]^T$ ensure the coupling between the components ε_{ij} and K_{ijkl}. The matrix $[C]$ is computed as

$$
[C]^T = \begin{bmatrix}
\left(c'_1+\cdots+c'_6\right) & \left(c'_1+c'_4\right) & \left(c'_1+c'_4\right) & & & \\
\left(c'_1+c'_2\right) & \left(c'_1+c'_3\right) & c'_1 & & & \\
\left(c'_4+c'_6\right)/\sqrt{2} & \left(c'_4+c'_5\right)/\sqrt{2} & c'_4/\sqrt{2} & & & \\
\left(c'_1+c'_4\right) & \left(c'_1+\cdots+c'_6\right) & \left(c'_1+c'_4\right) & & & \\
\left(c'_1+c'_3\right) & \left(c'_1+c'_2\right) & c'_1 & & & \\
\left(c'_4+c'_5\right)/\sqrt{2} & \left(c'_4+c'_6\right)/\sqrt{2} & c'_4/\sqrt{2} & & & \\
 & & & \left(c'_2+c'_6\right)/\sqrt{2} & & \\
 & & & \left(c'_2+c'_5\right)/\sqrt{2} & & \\
 & & & c'_3+\left(c'_5+c'_6\right)/\sqrt{2} & & \\
 & & & \left(c'_2+c'_6\right)/\sqrt{2} & & \\
 & & & \left(c'_2+c'_5\right)/\sqrt{2} & & \\
 & & & c'_3+\left(c'_5+c'_6\right)/\sqrt{2} & &
\end{bmatrix}.
\tag{115}
$$

Finally, the matrices $\left[H^a_\chi\right]$ and $\left[H^b_\chi\right]$,

$$
\begin{bmatrix} H^a_\chi \end{bmatrix} = \begin{bmatrix} H^a_\chi & & \\ & \ddots & \\ & & H^a_\chi \end{bmatrix}, \quad \begin{bmatrix} H^b_\chi \end{bmatrix} = \begin{bmatrix} H^b_\chi & & \\ & \ddots & \\ & & H^b_\chi \end{bmatrix},
\tag{116}
$$

are the diagonal matrices setting the internal constraint, presented in Appendix A.3, ensuring the equivalences (102) and enabling the second order micromorphic model to coincide with Mindlin's second strain gradient theory.

The last element that has to be discussed about the relation (111b) is the term $b_0[\underset{\approx}{\mathbf{1}}]$ appearing on the left-hand side. The

initial higher order stress, or cohesion modulus, b_0, is present in some components of the triple stress tensor $\underset{\approx}{\underset{\approx}{\boldsymbol{S}}}$. These components are identified in Eq. (99c) as having the form S_{kkll}, S_{klkl} and S_{kllk}, so that

$$b_0\left[\underset{\approx}{\underset{\approx}{\mathbf{1}}}\right]^T = \left[b_0 \;\; \tfrac{1}{3}b_0 \;\; \tfrac{\sqrt{2}}{3}b_0 \;\; b_0 \;\; \tfrac{1}{3}b_0 \;\; \tfrac{\sqrt{2}}{3}b_0 \;\; 0\;0\;0\;0\;0\;0\right]^T. \tag{117}$$

The principle of virtual work, in the absence of body forces, stipulates that, for all virtual $[DOF^*]$,

$$\int_V \left[\underset{\sim}{\boldsymbol{\sigma}}\colon \underset{\sim}{\boldsymbol{\varepsilon}}^* + \underset{\sim}{\boldsymbol{s}}\colon \underset{\sim}{\boldsymbol{e}}^* + \underset{\sim}{\underset{\sim}{\boldsymbol{S}}} \vdots \underset{\sim}{\underset{\sim}{\boldsymbol{K}}}^* + \underset{\sim}{\underset{\sim}{\boldsymbol{s}}} \vdots \underset{\sim}{\underset{\sim}{\boldsymbol{e}}}^* + \underset{\approx}{\underset{\approx}{\boldsymbol{S}}} :: \underset{\approx}{\underset{\approx}{\boldsymbol{K}}}^*\right] dV = \int_{\partial V}\left(\underset{\sim}{\boldsymbol{t}}.\,\underset{\sim}{\boldsymbol{u}}^* + \underset{\sim}{\underset{\sim}{\boldsymbol{t}}}\colon \underset{\sim}{\boldsymbol{\chi}}^* + \underset{\sim}{\underset{\sim}{\boldsymbol{t}}} \vdots \underset{\sim}{\underset{\sim}{\boldsymbol{\chi}}}^*\right) dS. \tag{118}$$

which can be translated into the following matrix form:

$$\int_V [STRESS]^T\left[STRAIN^*\right] dV = \int_{\partial V} [t]^T\left[DOF^*\right] dS \tag{119}$$

$$\int_V [STRAIN]^T\left[D\right]\left[STRAIN^*\right] dV = \int_{\partial V} [t]^T\left[DOF^*\right] dS \tag{120}$$

$$\int_V [DOF]^T\left[\mathrm{B}_{matrix}\right]^T\left[D\right]\left[\mathrm{B}_{matrix}\right]\left[DOF^*\right] dV = \int_{\partial V} [t]^T\left[DOF^*\right] dS. \tag{121}$$

The matrix form of the problem to solve then takes the usual form

$$[F] = [K][DOF], \tag{122}$$

with the generalised stiffness matrix,

$$\left[K\right] = \int_V \left[\mathrm{B}_{matrix}\right]^T\left[D\right]\left[\mathrm{B}_{matrix}\right] dV, \tag{123}$$

and

$$\left[F\right] = \int_{\partial V} [t]^T\, dS. \tag{124}$$

An incremental form of the algorithm is used so that the unknowns are the increment of *DOF*s, $\Delta[STRESS] = [D]\;\Delta[STRAIN]$ and b_0 does not arise in Eq. (120).

The $\sqrt{2}$ in $[STRESS]$ and $[STRAIN]$ are such that the chosen form of the power density of internal forces given in Eq. (87) is respected,

$$[STRESS]^T\left[STRAIN^*\right] = \sigma_{ij}\,\varepsilon^*_{ij} + s_{ij}\,e^*_{ij} + S_{ijk}\,K^*_{ijk} + s_{ijk}\,e^*_{ijk} + S_{ijkl}\,K^*_{ijkl}, \tag{125}$$

this is the reason why several coefficients of the matrices $[\mathrm{B}_{matrix}]$, $[C]$ and $b_0[\underset{\approx}{\underset{\approx}{\mathbf{1}}}]$ were multiplied by $(\sqrt{2})^{\pm 1}$ in order to fit this chosen form and to end up with the same relations as formulated in the second order micromorphic model. For example, the strains given in Eq. (91) remain

$$\begin{aligned} &\varepsilon_{ij} = \tfrac{1}{2}\left(u_{i,j} + u_{j,i}\right), \quad e_{ij} = \varepsilon_{ij} - \chi_{ij}, \quad K_{ijk} = \chi_{ij,k}, \\ &e_{ijk} = K_{ijk} - \chi_{ijk}, \quad K_{ijkl} = \chi_{ijk,l}, \end{aligned} \tag{126}$$

and more particularly, as the modified coefficients are related to ε_{ij}, e_{ij}, K_{ijk}, e_{ijk} and K_{ijkl} when $i \neq j$, we have

$$\sqrt{2}\;\varepsilon_{12} = \frac{u_{1,2}}{\sqrt{2}} + \frac{u_{2,1}}{\sqrt{2}} \;\equiv\; \varepsilon_{12} = \frac{1}{2}\left(u_{1,2} + u_{2,1}\right), \tag{127}$$

$$\sqrt{2}\;e_{121} = \sqrt{2}\;\chi_{12,1} - \sqrt{2}\;\chi_{121} = \sqrt{2}\;K_{121} - \sqrt{2}\;\chi_{121} \;\equiv\; e_{121} = K_{121} - \chi_{121}, \tag{128}$$

$$\sqrt{2}\;K_{1221} = \sqrt{2}\;\chi_{122,1} \;\equiv\; K_{1221} = \chi_{122,1}. \tag{129}$$

References

Agrawal, R., Peng, B., Gdoutos, E.E., Espinosa, H.D., 2008. Elasticity size effects in ZnO nanowires—a combined experimental–computational approach. Nano Lett. 8 (11), 3668–3674.

Altenbach, H., Eremeyev, V.A., 2011. On the shell theory on the nanoscale with surface stresses. Int. J. Eng. Sci. 49, 1294–1301.

Altenbach, H., Eremeyev, V.A., Lebedev, L.P., 2011. On the spectrum and stiffness of an elastic body with surface stresses. Z. Angew. Math. Mech. 91, 699–710.

Altenbach, H., Eremeyev, V.A., Morozov, N.F., 2012. Surface viscoelasticity and effective properties of thin-walled structures at the nanoscale. Int. J. Eng. Sci. 59, 83–89.
Amiot, F., 2013. An Euler–Bernoulli second strain gradient beam theory for cantilever sensors. Philos. Mag. Lett. 93, 204–212.
Auffray, N., 2014. Analytical expressions for odd-order anisotropic tensor dimension. C. R. Méc. 342, 284–291.
Auffray, N., dell'Isola, F., Eremeyev, V., Madeo, A., Rosi, G., 2013a. Analytical continuum mechanics à la Hamilton–Piola: least action principle for second gradient continua and capillary fluids. Mech. Math. Solids, http://dx.doi.org/10.1177/1081286513497616.
Auffray, N., Le Quang, H., He, Q.C., 2013b. Matrix representations for 3d strain-gradient elasticity. J. Mech. Phys. Solids 61, 1202–1223.
Besson, J., Cailletaud, G., Chaboche, J.-L., Forest, S., Blétry, M., 2009. Non-Linear Mechanics of Materials. Series: Solid Mechanics and Its Applications, vol. 167. Springer, 433 pp, ISBN: 978-90-481-3355-0.
Boehme, T., Dreyer, W., Mueller, W.H., 2007. Determination of stiffness and higher gradient coefficients by means of the embedded-atom method—an approach for binary alloys. Contin. Mech. Thermodyn. 18, 411–441.
Casal, P., 1961. La capillarité interne. Cah. Groupe Français d'Etudes Rhéol. 6, 31–37.
Casal, P., 1963. Capillarité interne en mecanique. C.R. Acad. Sci. Paris 256, 3820–3822.
Casal, P., 1972. La théorie du second gradient et la capillarité. C.R. Acad. Sci. Paris 274, 1571–1574.
Casal, P., Gouin, H., 1985. Relation entre l'équation de l'énergie et l'équation du mouvement en théorie de Korteweg de la capillarité. C. R. Séances Acad. Sci. Série 2, Méc. Phys. Chim. Sci. Univers. Sci. Terre 300, 231–234.
Chhapadia, P., Mohammadi, P., Sharma, P., 2011. Curvature-dependent surface energy and implications for nanostructures. J. Mech. Phys. Solids 59, 2103–2115.
Chhapadia, P., Mohammadi, P., Sharma, P., 2012. Erratum-Curvature-dependent surface energy and implications for nanostructures. J. Mech. Phys. Solids 60, 1241–1242.
Cordero, N.M., 2011. A Strain Gradient Approach to the Mechanics of Micro and Nanocrystals (Ph.D. thesis). Mines ParisTech.
Craighead, H.G., 2000. Nanoelectromechanical systems. Science 290 (5496), 1532–1535.
Danescu, A., 2012. Hyper-pre-stress vs. strain-gradient for surface relaxation in diamond-like structures. J. Mech. Phys. Solids 60, 623–642.
Danescu, A., Grenet, G., 2012. Continuum strain-gradient elasticity from discrete valence force field model for diamond-like crystals. Int. J. Fract. 174, 95–102.
Davydov, D., Javili, A., Steinmann, P., 2013. On molecular statics and surface-enhanced continuum modeling of nano-structures. Comput. Mater. Sci. 69, 510–519.
Dell'Isola, F., Seppecher, P., 1995. The relationship between edge contact forces, double forces and intersticial working allowed by the principle of virtual power. C.R. Acad. Sci. Paris IIb 321, 303–308.
Dell'Isola, F., Seppecher, P., 1997. Edge contact forces and quasi-balanced power. Meccanica 32, 33–52.
Dell'Isola, F., Seppecher, P., Madeo, A., 2012. How contact interactions may depend on the shape of Cauchy cuts in N-th gradient continua: approach "à la D'Alembert". Z. Angew. Math. Phys. 63, 1119–1141.
Dingreville, R., Abdelmalek, H., Berbenni, S., 2014. From coherent to incoherent mismatched interfaces: a generalized continuum formulation of surface stresses. J. Mech. Phys. Solids 72, 40–60.
Dingreville, R., Qu, J., Cherkaoui, M., 2005. Surface free energy and its effect on the elastic behavior of nano-sized particles, wires and films. J. Mech. Phys. Solids 53 (8), 1827–1854.
Dingreville, R., Qu, J.M., 2008. Interfacial excess energy, excess stress and excess strain in elastic solids: planar interfaces. J. Mech. Phys. Solids 56, 1944–1954.
Dormieux, L., Kondo, D., 2013. Non linear homogenization approach of strength of nanoporous materials with interface effects. Int. J. Eng. Sci. 71, 102–110.
Duan, H.L., Wang, J., Karihaloo, B.L., 2009. Theory of elasticity at the nanoscale. Adv. Appl. Mech. 42, 1–68.
Feng, X.L., He, R., Yang, P., Roukes, M.L., 2007. Very high frequency silicon nanowire electromechanical resonators. Nano Lett. 7 (7), 1953–1959.
Forest, S., 2009. The micromorphic approach for gradient elasticity, viscoplasticity and damage. ASCE J. Eng. Mech. 135, 117–131.
Forest, S., Aifantis, E.C., 2010. Some links between recent gradient thermo-elasto-plasticity theories and the thermomechanics of generalized continua. Int. J. Solids Struct. 47, 3367–3376.
Forest, S., Cordero, N.M., Busso, E.P., 2011. First vs. second gradient of strain theory for capillarity effects in an elastic fluid at small length scales. Comput. Mater. Sci. 50, 1299–1304.
Forest, S., Sievert, R., 2003. Elastoviscoplastic constitutive frameworks for generalized continua. Acta Mech. 160, 71–111.
Germain, P., 1973a. La méthode des puissances virtuelles en mécanique des milieux continus. Première partie: Théorie du second gradient. J. Méc. 12, 235–274.
Germain, P., 1973b. The method of virtual power in continuum mechanics. Part 2: microstructure. SIAM J. Appl. Math., 556–575.
Gu, S.T., Liu, J.T., He, Q.C., 2014. Size-dependent effective elastic moduli of particulate composites with interfacial displacement and traction discontinuities. Int. J. Solids Struct. 51, 2283–2296.
Gurtin, M.E., Murdoch, A.I., 1975. Continuum Theory of Elastic-Material Surfaces. Arch. Ration. Mech. Anal. 57, 291–323.
Gurtin, M.E., Murdoch, A.I., 1978. Surface stress in solids. Int. J. Solids Struct. 14, 431–440.
He, Q.C., Feng, Z.Q., 2012. Homogenization of layered elastoplastic composites: theoretical results. Int. J. Non-Linear Mech. 47, 367–376.
Hervé-Luanco, E., 2014. Elastic behavior of composites containing multi-layer coated particles with imperfect interface bonding conditions and application to size effects and mismatch in these composites. Int. J. Solids Struct. 51, 2865–2877.
Hoang, M.T., Yvonnet, J., Mitrushchenkov, A., Chambaud, G., 2013. First-principles based multiscale model of piezoelectric nanowires with surface effects. J. Appl. Phys. 113.
Javili, A., dell'Isola, F., Steinmann, P., 2013. Geometrically nonlinear higher-gradient elasticity with energetic boundaries. J. Mech. Phys. Solids 61, 2381–2401.
Javili, A., Kaessmair, S., Steinmann, P., 2014. General imperfect interfaces. Comput. Methods Appl. Mech. Eng. 275, 76–97.
Javili, A., McBride, A., Mergheim, J., Steinmann, P., Schmidt, U., 2013. Micro-to-macro transitions for continua with surface structure at the microscale. Int. J. Solids Struct. 50, 2561–2572.
Javili, A., McBride, A., Steinmann, P., Reddy, B., 2014. A unified computational framework for bulk and surface elasticity theory: a curvilinear-coordinate-based finite element methodology. Comput. Mech. 54, 745–762.
Javili, A., McBride, A., Steinmann, P., Reddy, B.D., 2012. Relationships between the admissible range of surface material parameters and stability of linearly elastic bodies. Philos. Mag. 92 (28–30), 3540–3563.
Javili, A., Steinmann, P., 2010. On thermomechanical solids with boundary structures. Int. J. Solids Struct. 47 (24), 3245–3253.
Javili, A., Steinmann, P., 2011. A finite element framework for continua with boundary energies. Part III: the thermomechanical case. Comput. Methods Appl. Mech. Eng. 200, 1963–1977.
Lazar, M., Maugin, G.A., Aifantis, E., 2006a. Dislocations in second strain gradient elasticity. Int. J. Solids Struct. 43, 1787–1817.
Lazar, M., Maugin, G.A., Aifantis, E.C., 2006b. On a theory of nonlocal elasticity of bi-Helmholtz type and some applications. Int. J. Solids Struct. 43, 1404–1421.
Magoariec, H., Danescu, A., 2009. Modeling macroscopic elasticity of porous silicon. In: Nassiopoulou, A., Sailor, M., Canham, L., Schmuki, P. (Eds.), Physica Status Solidi C, vol. 6. pp. 1680–1684.
Maranganti, R., Sharma, P., 2007. A novel atomistic approach to determine strain-gradient elasticity constants: tabulation and comparison for various metals, semiconductors, silica, polymers and the (ir) relevance for nanotechnologies. J. Mech. Phys. Solids 55, 1823–1852.
Marcadon, V., Brown, D., Hervé, E., Mele, P., Alberola, N.D., Zaoui, A., 2013. Confrontation between Molecular Dynamics and micromechanical approaches to investigate particle size effects on the mechanical behaviour of polymer nanocomposites. Comput. Mater. Sci. 79, 495–505.
Marcadon, V., Hervé, E., Zaoui, A., 2007. Micromechanical modeling of packing and size effects in particulate composites. Int. J. Solids Struct. 44, 8213–8228.

McDowell, M.T., Leach, A.M., Gall, K., 2008. Bending and tensile deformation of metallic nanowires. Model. Simul. Mater. Sci. Eng. 16, 045003.
Mindlin, R.D., 1964. Micro-structure in linear elasticity. Arch. Ration. Mech. Anal. 16 (1), 51–78.
Mindlin, R.D., 1965. Second gradient of strain and surface-tension in linear elasticity. Int. J. Solids Struct. 1, 417–438.
Mindlin, R.D., Eshel, N.N., 1968. On first strain gradient theories in linear elasticity. Int. J. Solids Struct. 4, 109–124.
Mitrushchenkov, A., Chambaud, G., Yvonnet, J., He, Q.C., 2010. Towards an elastic model of wurtzite AlN nanowires. Nanotechnology 21.
Mohammadi, P., Liu, L.P., Sharma, P., Kukta, R.V., 2013. Surface energy, elasticity and the homogenization of rough surfaces. J. Mech. Phys. Solids 61, 325–340.
Müller, P., Saúl, A., 2004. Elastic effects on surface physics. Surf. Sci. Rep. 54 (5–8), 157–258.
Ojaghnezhad, F., Shodja, H.M., 2013. A combined first principles and analytical determination of the modulus of cohesion, surface energy, and the additional constants in the second strain gradient elasticity. Int. J. Solids Struct. 50, 3967–3974.
Olive, M., Auffray, N., 2013. Symmetry classes for even-order tensors. Math. Mech. Complex Syst. 1, 177–210.
Olive, M., Auffray, N., 2014. Symmetry classes for odd-order tensors. Z. Angew. Math. Mech. 94, 421–447.
Polizzotto, C., 2013. A second strain gradient elasticity theory with second velocity gradient inertia—Part I: constitutive equations and quasi-static behavior. Int. J. Solids Struct. 50, 3749–3765.
Ru, C., Aifantis, E., 1993. A simple approach to solve boundary value problems in gradient elasticity. Acta Mech. 101, 59–68.
Sadeghian, H., Yang, C.K., Goosen, J.F.L., Van der Drift, E., Bossche, A., French, P.J., Van Keulen, F., 2009. Characterizing size-dependent effective elastic modulus of silicon nanocantilevers using electrostatic pull-in instability. Appl. Phys. Lett. 94, 221903.
Sanii, B., Ashby, P.D., 2010. High sensitivity deflection detection of nanowires. Phys. Rev. Lett. 104 (14), 147203.
Shodja, H.M., Ahmadpoor, F., Tehranchi, A., 2012. Calculation of the additional constants for fcc materials in second strain gradient elasticity: behavior of a nano-size Bernoulli–Euler beam with surface effects. J. Appl. Mech.—Trans. ASME 79, 021008.
Shu, J., 1998. Scale-dependent deformation of porous single crystals. Int. J. Plast. 14, 1085–1107.
Thomas, O., Ponchet, A., Forest Editors, S., 2011. Mechanics of Nano-objects. Presses des Mines, Paris, 380 pp, ISBN: 978-2911256-67-7.
Toupin, R.A., 1962. Elastic materials with couple-stresses. Arch. Ration. Mech. Anal. 11 (1), 385–414.
Upadhyay, M.V., Capolungo, L., Taupin, V., Fressengeas, C., 2012. Elastic constitutive laws for incompatible crystalline media: the contributions of dislocations, disclinations and G-disclinations. Philos. Mag. 93, 794–832.
Villain, P., Beauchamp, P., Badawi, K.F., Goudeau, P., Renault, P., 2004. Atomistic calculation of size effects on elastic coefficients in nanometre-sized tungsten layers and wires. Scr. Mater. 50, 1247–1251.
Yvonnet, J., Le Quang, H., He, Q.C., 2008. An XFEM/level set approach to modelling surface/interface effects and to computing the size-dependent effective properties of nanocomposites. Comput. Mech. 42, 119–131.
Yvonnet, J., Mitrushchenkov, A., Chambaud, G., He, Q.C., 2011. Finite element model of ionic nanowires with size-dependent mechanical properties determined by ab initio calculations. Comput. Methods Appl. Mech. Eng. 200, 614–625.
Yvonnet, J., Mitrushchenkov, A., Chambaud, G., He, Q.C., Gu, S.T., 2012. Characterization of surface and nonlinear elasticity in wurtzite ZnO nanowires. Journal of Applied Physics, 111.
Zhang, X., Sharma, P., 2005. Inclusions and inhomogeneities in strain gradient elasticity with couple stresses and related problems. International Journal of Solids and Structures 42, 3833–3851.